J. Fluid Mech. (2002), *vol.* 450, *pp.* 67–95.
DOI: 10.1017/S0022112001006267 Printed in the United Kingdom

The two-sided lid-driven cavity: experiments on stationary and time-dependent flows

By CH. BLOHM AND H. C. KUHLMANN

ZARM - University of Bremen, 28359 Bremen, Germany

(Received 20 November 2000 and in revised form 2 July 2001)

The incompressible fluid flow in a rectangular container driven by two facing sidewalls which move steadily in anti-parallel directions is investigated experimentally for Reynolds numbers up to 1200. The moving sidewalls are realized by two rotating cylinders of large radii tightly closing the cavity. The distance between the moving walls relative to the height of the cavity (aspect ratio) is $\Gamma = 1.96$. Laser-Doppler and hot-film techniques are employed to measure steady and time-dependent vortex flows. Beyond a first threshold robust, steady, three-dimensional cells bifurcate supercritically out of the basic flow state. Through a further instability the cellular flow becomes unstable to oscillations in the form of standing waves with the same wavelength as the underlying cellular flow. If both sidewalls move with the same velocity (symmetrical driving), the oscillatory instability is found to be tricritical. The dependence on two sidewall Reynolds numbers of the ranges of existence of steady and oscillatory cellular flows is explored. Flow symmetries and quantitative velocity measurements are presented for representative cases.

1. Introduction

Vortex flows in closed systems are of fundamental interest and of practical importance. To study their general properties, isothermal flows are frequently considered in the simplified model of a lid-driven cavity (Koseff & Street 1984*a*). This model is related to several technical applications such as short-dwell coating (Aidun & Triantafillopoulos 1997; Triantafillopoulos & Aidun 1990), continuous drying (Alleborn, Raszillier & Durst 1999), or the flow in gate slots of water-reservoir dam-gates whose performance depends on the slot geometry (Vischer & Hager 1998). The lid-driven cavity has also been studied, with side heating, in the context of transport processes in lakes (Stefanovic & Stefan 2000). In addition to these applications, the model has become a standard benchmark problem for two- and three-dimensional Navier–Stokes solvers (Deville, Lê & Morchoisne 1992).

The lid-driven cavity is a rectangular container which is typically filled with a Newtonian liquid. While one sidewall moves with a constant velocity tangentially to itself and parallel to the edges of the container, the remaining sidewalls are at rest. The present experimental study is aimed at extending the range of phenomena accessible by this classical configuration with a single moving lid. To that end we use an apparatus that allows the independent motion of two opposing sidewalls. This configuration enables the realization of different types of vortex flows and, hence, other types of flow instabilities not observable in the single-lid-driven cavity.

Most previous investigations have been carried out for the one-sided lid-driven cavity with square cross-section for which the width d equals the height h. Then the

cross-sectional aspect ratio is unity, $\Gamma = d/h = 1$. The spanwise aspect ratio $\Lambda = l/h$, defined as the spanwise length l to the height h, was either $\Lambda = 1$ or $\Lambda = 3$.

The first thorough theoretical and numerical investigation of the one-sided lid-driven cavity problem is due to Burggraf (1966). Around the the same time, Pan & Acrivos (1967) numerically investigated the structure of the primary flow for $Re = 0$ and compared their experimental results with the theoretical ones of Burggraf (1966) for Reynolds numbers up to $Re = Uh/\nu = 4000$, where U is the velocity of the lid and ν the kinematic viscosity. Koseff & Street (1984*a*, *b*, *c*), Koseff *et al.* (1983), Freitas *et al.* (1985), and Prasad & Koseff (1989) carried out a series of numerical and experimental investigations for Reynolds numbers in the range $1000 \leqslant Re \leqslant 10\,000$. The flow was found to be three-dimensional and it essentially consisted of a single main vortex, superimposed with time-dependent three-dimensional secondary eddies, if the Reynolds number is sufficiently high. Rhee, Koseff & Street (1984) visualized the flow for $Re \geqslant 2000$ and reported the existence of unsteady Taylor–Görtler-like vortices in the region close to the downstream corner eddy. Endwall effects have been considered by Koseff & Street (1984*b*) and Prasad & Koseff (1989). The influence of the finite container length on the flow was assessed by varying the spanwise aspect ratio in the range $\Lambda \leqslant 3$.

More recently, Aidun, Triantafillopoulos & Benson (1991) studied a one-sided lid-driven square-cavity ($\Gamma = 1$) with spanwise aspect ratio $\Lambda = 3$ for $100 \leqslant Re \leqslant 2000$. Their apparatus allowed a small amount of through-flow to enter the cavity from the rigid corner upstream of the moving wall and to leave the cavity through the downstream corner of the moving lid. As the first instability of the primary flow they found small-amplitude time-periodic waves at $Re \approx 825$. These waves appeared as spiral-shaped vortices originating from the midplane of the cavity (perpendicular to the primary-vortex axis) and travelling symmetrically outward towards the endwalls. Furthermore, they discovered stationary three-dimensional vortex flows which filled the whole cavity after the Reynolds number is suddenly decreased from $Re \approx 2000$ to $Re \leqslant 500$. In a follow-up, the onset of oscillatory flow in the same apparatus has been investigated by Benson & Aidun (1992) by means of a wall-mounted hot-film probe. For $Re \gtrsim 900$ the authors confirmed the existence of the time-periodic state found by Aidun *et al.* (1991). A further increase of the Reynolds number led to quasi-periodic and chaotic flows. A recent review of the one-sided lid-driven cavity problem has been given by Shankar & Deshpande (2000).

To clarify the nature of the first instability a number of linear stability analyses have been carried out using periodic boundary conditions in the spanwise direction. Ramanan & Homsy (1994) and Ding & Kawahara (1998, 1999) numerically investigated the stability of the two-dimensional basic flow in the one-sided lid-driven cavity in the limit $\Lambda \to \infty$. While these authors missed the true critical Reynolds number, Albensoeder, Kuhlmann & Rath (2001*b*) recently calculated the correct linear stability boundary. They showed that the first instability in the square cavity occurs at $Re_c = 786$, a result which they also confirmed experimentally in a modification of the setup used by Kuhlmann, Wanschura & Rath (1997). It was argued that the large critical wavenumber of the critical mode $k_c = 15.4$ (in units of the inverse cavity height) was the reason why previous investigations missed the linear-stability boundary, and that the small spanwise aspect ratio $\Lambda = 3$ used by Aidun *et al.* (1991) and Benson & Aidun (1992) prevented them from observing the first, steady instability in their experiment. Moreover, Albensoeder *et al.* (2001*b*) considered the whole range of aspect ratios Γ and found four different types of instability which are all caused by centrifugal effects.

The first investigation of the nonlinear flow in two-sided lid-driven cavities in which both walls move in opposite directions is due to Kuhlmann *et al.* (1997). They experimentally studied different two- and three-dimensional flows in an apparatus where the separation between the two moving walls was approximately twice the height of the cavity ($\Gamma = 1.96$). The spanwise aspect ratio was $\Lambda = 6.55$. Their experiments were supplemented by linear-stability analyses for varying aspect ratio Γ and for $\Lambda \to \infty$. It was found numerically that the two-dimensional flows are not unique. This result was confirmed by the experimental observation of hysteresis between two different quasi-two-dimensional cavity flows. While one flow state consists of two well-separated vortices, the vortices are partly merged in the other state. The linear-stability analysis showed that the merged-vortex flow becomes three-dimensional through the elliptical instability mechanism proposed by Pierrehumbert (1986) and Bayly (1986). This instability is caused by the large strain rates associated with the high eccentricity of the closed streamlines (Kuhlmann *et al.* 1997; see also Kuhlmann, Wanschura & Rath 1998). The numerically predicted instability was confirmed by experiments carried out in parallel. They revealed the supercritical flow pattern as a row of steady rectangular cells within each of which the flow is three-dimensional.

Albensoeder, Kuhlmann & Rath (2001*a*) extended the results of Kuhlmann *et al.* (1997) on the non-uniqueness of the two-dimensional flows in the two-sided lid-driven cavity. Their numerical calculations covered the parameter space spanned by the two sidewall Reynolds numbers and the aspect ratio Γ in the range $|Re_{1,2}| \leqslant 700$ and $\Gamma \in [0.2, 3.0]$. Depending on the exact parameter values up to seven different non-trivial flow states were found to exist for given values of Re_1, Re_2 and Γ. The stability of these flow states, however, was not addressed by Albensoeder *et al.* (2001*a*).

The present paper is an extension of the work of Kuhlmann *et al.* (1997). Here we investigate the supercritical three-dimensional cellular flow in a cavity with aspect ratio $\Gamma = 1.96$. The experimental setup is introduced in § 2. Section 3 deals with symmetry properties, quantitative velocity fields, and existence ranges of the steady cellular flow. The onset to time-dependent cellular flow is treated in § 4, where we analyse symmetries, existence boundaries, and bifurcation diagrams. The results are summarized in § 5.

2. Experimental setup and measurement techniques

A nearly rectangular cavity is formed by four stationary plane rigid walls and two facing sidewalls, realized as chrome-plated metal cylinders of large radii $R_1 = 87.55\,\text{mm}$ and $R_2 = 88.25\,\text{mm}$. The cylinders allow a tangential wall motion by rotation about their axes. The geometry and coordinate system are sketched in figure 1. The same device has been employed by Kuhlmann *et al.* (1997). Compared to that setup the four stationary walls have been rebuilt for better optical accessibility. The average value of the minimum ($d_{\min} = 55.4\,\text{mm}$) and maximum ($d_{\max} = 57.9\,\text{mm}$) distances in the x-direction between the cylinders is referred to as width $d = 56.7\,\text{mm}$. The height in the y-direction and the length of the cavity in the z-direction are $h = 29.0\,\text{mm}$ and $l = 190\,\text{mm}$, respectively. Scaling all lengths with the cavity height h the geometry is defined by the aspect ratios in the (x, y)- (cross-sectional aspect ratio Γ) and (y, z)-plane (spanwise aspect ratio Λ),

$$\Gamma = \frac{d}{h} = 1.96 \pm 0.05, \quad \Lambda = \frac{l}{h} = 6.55 \pm 0.03. \tag{2.1}$$

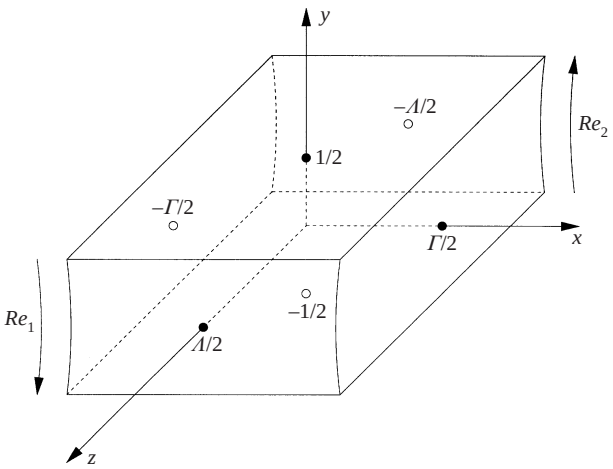

FIGURE 1. Geometry and coordinate system of the cavity.

The top and the bottom of the cavity at $y = \pm 1/2$ as well as the endwalls at $z = \pm \Lambda/2$ are made of Perspex. For visualization purposes the bottom plate at $y = -1/2$ is painted black.

The fluid is set into motion by independently rotating each cylinder about its axis with a constant angular velocity. Each cylinder is driven via tooth belts by its own computer-controlled permanent-magnet synchronous motor. The whole cavity, including the rotating cylinders, is mounted inside an outer container and immersed into the working fluid, which is Bayer Baysilone M20 silicone oil of kinematic viscosity $\nu_0 = 22.2\,\mathrm{mm^2\,s^{-1}}$ and density $\rho_0 = 0.956\,\mathrm{g\,mm^{-3}}$ at 20 °C. The temperature in the cavity, which had a volume of ≈ 0.3 l, and in the outer bath with a capacity of ≈ 15 l changed only slowly during the experiments, typically less than $0.05\,^{\circ}\mathrm{C\,h^{-1}}$. Because the outer bath is well stirred by the rotating cylinders, the cavity can be considered isothermal to high accuracy. To keep the sidewall Reynolds numbers

$$Re_i = \frac{\Omega_i R_i h}{\nu} \tag{2.2}$$

at constant values, the angular velocities Ω_i $(i = 1, 2)$ are periodically adjusted every 60 s to the instantaneous value of the viscosity which is determined by measuring the temperature of the fluid by a thermocouple (PT100). The gauge curve $\nu(T)$ was previously measured independently, with an absolute accuracy of $\Delta\nu = \pm 0.05\,\mathrm{mm^2\,s^{-1}}$. The actual viscosity is calculated using an exponential fit of the measured gauge data. The flow inside the cavity is visualized using a bright ≈ 7 mm thick halogen light sheet and suspending particles in the liquid. Polyamide-12 particles of nearly spherical shape were used for streakline photographs. Their density and mean diameter are $\rho = 1.016\,\mathrm{g\,mm^{-3}}$ and $d_{\mathrm{p1}} \approx 57\,\mu\mathrm{m}$, respectively. Fine aluminium flakes of thickness 10 to 15 μm and diameter up $\approx 150\,\mu\mathrm{m}$ have been used for observations by the naked eye, because their non-isotropic reflectivity allows a better identification of flow patterns than the nearly isotropically reflecting Polyamide-12 particles.

Quantitative measurements of the flow were made using two different techniques. Steady and time-dependent flow fields were measured by laser-Doppler velocimetry (LDV) using a Dantec velocimeter (model *Flowlite*), the optical system of which has an aperture of 38 mm and a focal length of 160 mm. Again, seeding with Polyamide-

12 particles was employed. These had the same density as those for visualization, but a mean diameter of $d_{p2} \approx 5\,\mu m$ which is of the order of magnitude of the interference-fringe distance ($\approx 3.8\,\mu m$). In addition, two hot-film probes (TSI model 1237) were flush mounted to the bottom wall of the cavity at $\boldsymbol{x}_a = (0, -1/2, 0)$ and at $\boldsymbol{x}_b = (0, -1/2, \Lambda/8)$. This technique was mainly used for time-dependent oscillatory flows, where it allows the quantitative measurement of discrete frequencies. Moreover, the amplitudes of the oscillating shear stress on the wall as functions of the Reynolds numbers can be determined up to a constant factor, as long as the oscillation amplitudes are sufficiently small, i.e. as long as the output signal can be linearized with respect to the shear-stress fluctuations.

The hot-film data were acquired using a transient recorder (Nicolet model 460). They were analysed by fast Fourier and discrete Fourier transforms. To determine the frequencies and amplitudes of the spectral components of the oscillating-flow velocities measured by LDV we used a Lomb periodogram (Lomb 1976; Press *et al.* 1992) based on a least-squares fitting of unevenly sampled time-series data. This method has been employed before, e.g. by Wulf, Egbers & Rath (1999) to analyse laser-Doppler measurements of spherical Couette flow.

During all experiments reported in the following, both cylinders were rotated in the same sense. Hence, the cavity sidewalls move in opposite directions. All velocity data $\boldsymbol{u} = (u, v, w)$, where u, v, and w denote the velocity components in the directions x, y, and z, respectively (see figure 1), are made dimensionless by v/h. As the time scale we use h^2/v. The error of the velocity measurements is estimated to be less than the maximum standard deviation that occurred during the LDV measurements $\Delta u \cong \Delta v \cong \Delta w \cong \pm 1.5$, in non-dimensional units.

3. Steady three-dimensional flows

The lid-driven flow in finite-length cavities is always three-dimensional, even if the span is large. The secondary three-dimensional flow (called Ekman or Bödewadt flow) induced by the endwalls at $z = \pm\Lambda/2$ perpendicular to the axis of the main vortex is well known (Bödewadt 1940). In many previous experiments (e.g. Koseff & Street 1984*c*; Aidun *et al.* 1991) the spanwise aspect ratio was $\Lambda = 3$. Even though the length is three times the cavity height, the value $\Lambda = 3$ must be considered small, because the three-dimensional flow effects are considerable throughout the whole cavity and may thus prevent the observation of certain bulk-flow instabilities (Albensoeder *et al.* 2001*b*). Three-dimensional effects are also important in the present setup with $\Lambda = 6.55$. However, the deviations from a two-dimensional flow are much smaller in the centre of the cavity around $z = 0$ than for $\Lambda = 3$. A comparison between the experimentally determined streaklines in steady flow ($\Lambda = 6.55$) and the corresponding numerically calculated two-dimensional flow shows a very good agreement (Kuhlmann *et al.* 1997).

By numerical and experimental investigations, Kuhlmann *et al.* (1997) have shown that the nearly two-dimensional flow in a cavity with $\Gamma = 1.96$ and $\Lambda = 6.55$ undergoes an instability caused by the strong straining of the basic-flow streamlines. The present work extends their results and further analyses the three-dimensional flows beyond the first instability.

3.1. *General flow characteristics when* $Re = Re_1 = Re_2$

Consider the case of equal Reynolds numbers. The use of Re without a subscript indicates that both Reynolds numbers are the same: $Re = Re_1 = Re_2$. At low

Reynolds numbers and apart from weak three-dimensional endwall perturbations, Kuhlmann *et al.* (1997) found a two-dimensional flow which they called *two-vortex flow*, because it consists of two well-separated co-rotating vortices. On an increase of the Reynolds numbers the two-vortex flow undergoes a jump transition to a different two-dimensional flow which we shall call *strongly-merged-vortex flow* (Albensoeder *et al.* 2001*a*); this was called *cat's-eye flow* by Kuhlmann *et al.* (1997). In the strongly-merged-vortex state for $\Gamma = 1.96$ two smaller eddies are embedded in a globally recirculating flow. The separatrix streamline forms a hyperbolic stagnation point in the centre of the cavity (see figure 3 of Kuhlmann *et al.* (1997)).

The strongly-merged-vortex flow becomes three-dimensional via a supercritical bifurcation to a stationary flow consisting of rectangular cells. According to Kuhlmann *et al.* (1997) the three-dimensional flow first appears during a quasi-steady increase of the Reynolds numbers at $Re = 260$ in the form of a single rectangular cell (their figure 9) corresponding to a wavenumber $k = 2.2$ in the centre of the cavity. For $Re \geqslant 280$ four rectangular convection cells filling the whole cavity were observed. It was shown that, in addition to this four-cell flow, a five-cell flow exists above a certain Reynolds number. The boundaries between neighbouring convection cells have been identified as planes of constant z on which the spanwise velocity component w vanishes.

The existence of the single convection cell at $Re = 260$ is not observed in the present, rebuilt experimental setup. All other flow features reported by Kuhlmann *et al.* (1997) and mentioned above are confirmed by the present investigation. Visualizations of the four- and five-cell flows by tracer-particle streaks are shown in figure 2. The cellular flow in the centre of the cavity appears to be approximately periodic, one period in the z-direction comprising two cells. Kuhlmann *et al.* (1997) have calculated the stationary critical mode with wavenumber $k_c = 2\pi/\lambda_c = 2.25$ for $\Lambda \to \infty$. The theoretical critical mode is invariant under discrete translations, $z \to z + n\lambda_c$ ($n \in \mathbb{Z}$), reflections at the cell boundaries, $(x, y, z, u, v, w) \to (x, y, -z, u, v, -w)$, where the origin of the z-axis is taken on a cell boundary such that $w(x, y, z = 0) = 0$, and under half-wavelength translations $z \to z + (2n + 1)\lambda_c/2$ combined with a rotation by π about the z-axis $(x, y, z, u, v, w) \to (-x, -y, z, -u, -v, w)$. This leads to the invariance of the flow under

$$[x, y, z + (2n + 1)\lambda_c/4, u, v, w] \quad \longrightarrow \quad -[x, y, z + (2n + 1)\lambda_c/4, u, v, w]. \tag{3.1}$$

Hence, the neutral velocity field within a single cell must be point symmetric with respect to the centre of each cell located at $\boldsymbol{x}_n = (x_n, y_n, z_n) = (0, 0, (2n+1)\lambda_c/4)$. Since the full nonlinear Navier–Stokes equations in infinitely long systems ($\Lambda \to \infty$) also satisfy the same symmetry $[(\nabla, \boldsymbol{u}, p, t) \to (-\nabla, -\boldsymbol{u}, p, t)]$, there is no obvious reason, other than a spontaneous symmetry breaking, why this symmetry also applies to the nonlinear finite-amplitude three-dimensional flow in a certain range of supercritical Reynolds numbers.

Despite the endwall effects, these symmetries are observed to high accuracy for the finite-amplitude cells in the centre of the cavity (see e.g. figure 2). Note that a pure rotation of the pattern by π about the z-axis, which is compatible with the experimental boundary conditions ($Re_1 = Re_2$), leads to a different flow state. Hence, two different, though equivalent, flows states exist for a given number of cells (compare figures 2*a*, *b* and 2*c*, *d*).

Based on the favourable comparison between the measured and calculated stability boundaries and three-dimensional flow structures, including the wavenumber and the time-dependence, provided by Kuhlmann *et al.* (1997) we conclude that the

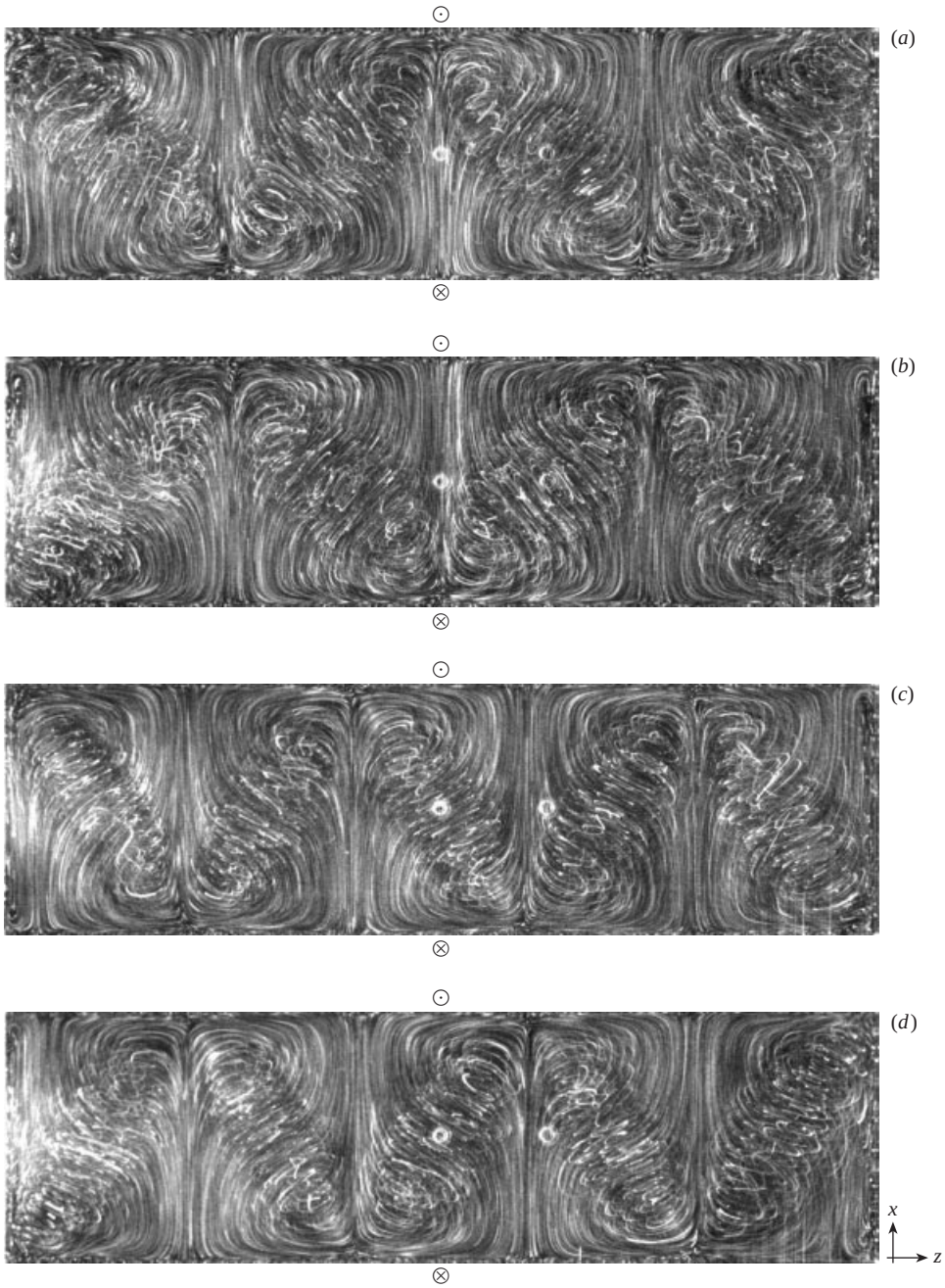

FIGURE 2. Streaklines of tracer particles in different steady three-dimensional flows for $Re = 700$: (*a*) four-cell V-mode, (*b*) four-cell Λ-mode, (*c*) five-cell V-mode, (*d*) five-cell Λ-mode. The streaklines have a considerable z-component near the walls at $x = \pm\Gamma/2$, because the light sheet, centred at $y = 0$, is relatively thick. Moreover, the spanwise velocity is high even close to the moving walls and a tiny fraction of the full view has been clipped near the top and bottom of each figure. The exposure time of the photographs was 1/4 s. The symbols ⊙ and ⊗ indicate the motion of the walls. In the centre and slightly to the right from there, one can see light reflections from the hot-film probes located at the bottom of the cavity.

instability is due to the elliptical mechanism (Pierrehumbert 1986; Bayly 1986). The same mechanism destabilizes Tollmien–Schlichting waves in plane channels or in viscous boundary layers (Bayly, Orszag & Hebert 1988). In fact, the observed cellular patterns have a similar structure to the transient Λ-vortices which develop on the unstable Tollmien–Schlichting waves (see e.g. Herbert 1988). Therefore, the cellular flows may be called *stationary Λ-vortices*. In order to distinguish between the two possible orientations of the Λ structure relative to the laboratory frame, we shall call the modes in figures 2*a*, *c* V-*modes*, while the flows shown in figures 2*b*, *d* are denoted Λ-*modes*, corresponding to the orientation of the apparent vortex centres within the two leftmost cells next to the wall at $z = -\Lambda/2$.

3.2. *Four-cell flow*

To investigate the bifurcation from the basic flow to the cellular flow the equilibrium amplitudes of the cellular flow have been measured as functions of the Reynolds numbers. To ensure that the flow is always in an equilibrium state, all experiments were carried out under quasi-steady conditions. The Reynolds numbers were varied in steps of $\Delta Re_i = 1$ after time lags Δt corresponding to the momentum-diffusion time across the relevant length scale. While for two-dimensional flows a time step of $\Delta t = 150\,\mathrm{s} \approx \tau_d = d^2/\nu$ would have sufficed, a time step of $\Delta t = 30\,\mathrm{min} \approx \tau_l = l^2/\nu$ has been employed for cellular-flow measurements. Accordingly, the equivalent ramping rate (here we use discrete steps) in the latter case was $\mathrm{d}Re_i/\mathrm{d}t = 5.6 \times 10^{-4}\,\mathrm{s}^{-1}$ which leads to a dimensionless ramp $r_i = (h^2/\nu_0)\,\mathrm{d}Re_i/\mathrm{d}t = 0.021$.

3.2.1. *Equal Reynolds numbers, $Re = Re_1 = Re_2$*

The bifurcation diagram for the instability of the strongly-merged-vortex flow to the three-dimensional four-cell flow for equal Reynolds numbers is shown in figure 3. The data for the V-mode have been obtained by LDV measurements of w at a fixed point in the flow during a quasi-steady increase of the Reynolds numbers. For the Λ-mode the Reynolds numbers have been decreased quasi-steadily. The velocity data indicate a supercritical pitchfork bifurcation.

On a quasi-steady increase of the Reynolds numbers the V-mode is always selected. However, the Λ-mode can be realized, in the present experimental setup, by keeping Re_1 constant in the range $300 \leqslant Re_1 \leqslant 800$ and increasing Re_2 quasi-steadily from zero to $Re_2 = Re_1$. For decreasing Reynolds numbers, keeping $Re_1 = Re_2$, we then find that the Λ-mode is replaced by the V-mode at $Re = 296 \pm 2\%$. During the transient process, the cells of the Λ-mode move slowly in the negative z-direction and one end cell becomes squeezed. After approximately 20 minutes the end cell adjacent to $z = -\Lambda/2$ disappears and a new cell is created at the other end of the cavity at $z = \Lambda/2$.

Due to the endwall-induced three-dimensional flow for $\Lambda = 6.55$ the z-component of the basic flow is not exactly zero at the monitoring point $z = -0.1\Lambda \neq 0$ in figure 3. Therefore, the measured velocity for subcritical Re is slightly biased towards negative values. This effect of the location of the monitoring point does not, however, explain the premature breakdown of the Λ-mode. Since the geometry and boundary conditions as well as the subcritical and supercritical flows including finite-span effects should be invariant under a rotation by π about the z-axis, the bifurcating flow branches in figure 3 should be symmetric with respect to $w = 0$ when the monitoring point lies on the line $x = y = 0$. Therefore, the observed preference for the V-mode can only be caused by imperfect endwall conditions (e.g. asymmetric leaks).

Apart from the observed imperfection, the bifurcation to the four-cell modes is

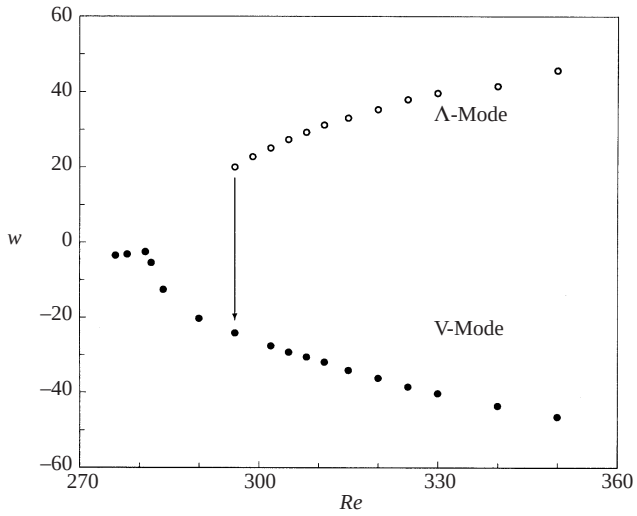

FIGURE 3. Spanwise velocity w in units of v/h at $(x, y, z) = (-0.245\Gamma, -0.252, -0.1\Lambda)$ as function of the Reynolds number. The two supercritical branches correspond to the four-cell V- and Λ-modes as indicated.

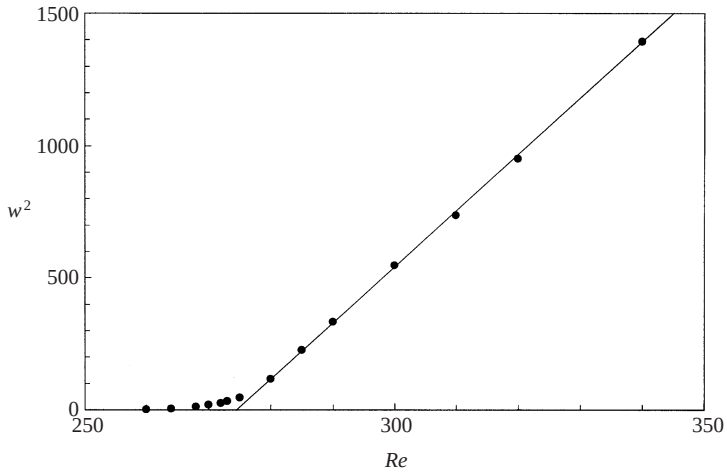

FIGURE 4. Squared lengthwise velocity w^2 in units of $(v/h)^2$ at $(x, y, z) = (0, 0.266, 0.132\Lambda)$ as function of the Reynolds number during a decrease of Re. The linear slope indicates a supercritical pitchfork bifurcation at $Re_c^{(1)} = 275$ for the onset of the steady three-dimensional four-cell V-mode. The smeared data near the critical point may be due to the imperfection provided by the endwall-induced Bödewadt flow and only partly due to the critical slowing down.

of supercritical pitchfork-type, because the cell amplitude increases almost with the square-root of the distance from the critical point $w \propto \pm(Re - Re_c^{(1)})^{1/2}$. This is clearly shown in figure 4 from which a critical Reynolds number $Re_c^{(1)} = 275 \pm 2\%$ is obtained by linear extrapolation of w^2 to zero. The range of Re within which the amplitude is well approximated by a square-root law extends up to 25% of $Re_c^{(1)}$ above the critical point.

We find that the two inner cells grow, while the two outer cells decrease in size when the Reynolds number Re is increased. The wavenumber corresponding to both inner cells decreases rapidly from $k_i = 2.16 \pm 0.04$ at $Re = 300$ to $k_i = 2.03 \pm 0.04$

at $Re = 400$. For larger Re the decrease is much weaker and $k_i = 1.96 \pm 0.04$ at $Re = 800$.

In order to further quantify the steady velocity fields, LDV measurements were made in planes $z = z_2$, where z_2 denotes the z-coordinate of the centre of the second cell from the left in figure 2(a). Since z_2, as well as k_i, depends slightly on Re, the centre of the cell has been determined prior to the measurement for each Reynolds number by locating both cell boundaries. In figure 5 the u-component of the velocity field is shown as a function of the normalized width x/Γ (a) and height y (b) for different Reynolds numbers. For increasing Reynolds numbers the extrema of u are shifted towards the boundaries. Besides this effect, the measured data confirm the point symmetry of the flow in the plane $z = z_2 = \text{const.}$ through the centre of the cell. In particular, $u(x = y = 0) = 0$.

The flow symmetry and the development as Re increases is demonstrated in figure 6. In the slightly supercritical four-cell flow (V-mode) shown in figure 6(a) the dependence $u(0, 0, z)$ is nearly harmonic in the centre of the cavity. Only the end cells are strongly distorted owing to the no-slip conditions at $z = \pm\Lambda/2$. The z-dependence of the strongly nonlinear four-cell flow is shown in figure 6(b). The velocity varies very strongly in a small vicinity of the rigid endwalls and the bulk flow exhibits much more structure. The point symmetry within the two interior cells is slightly violated in this example, because the data were taken slightly off from the centreline.

The flow in a cross-section $z = \text{const.}$ separates from the stationary top and bottom walls for Reynolds numbers $Re \gtrsim 600$. The separation of the three-dimensional flow is evident from figure 7, showing streaklines of a four-cell flow in the plane at $z \approx \Lambda/8$ (centre of a cell) for $Re = 800$. Small secondary vortices in the flow approaching the upstream corners of the moving walls can be seen in the upper left and lower right corners of the figure. Just before reaching the moving wall, the flow reattaches to the rigid wall. This behaviour is similar to that in the classical square cavity, where it occurs for Reynolds numbers above $Re = 1000$ (Benjamin & Denny 1979). The flow separation also leaves its traces on the pattern of ground tracer particles deposited on the stationary bottom wall, shown in figure 8. The streaks in the lower part of the photograph represent the direction field of the flow in the immediate vicinity of the solid wall at $y = -1/2$. In the upper part of the figure, where the visible streaks end, the flow has separated from the bottom. Generally, both the basic strongly-merged vortex flow and the three-dimensional cellular perturbation flow change with Reynolds number. While the streakline projections near the centres of the cells (figure 7) are very similar to the streamlines of the basic flow at $Re = 800$ (figure 3c of Kuhlmann *et al.* 1997), which likewise exhibits flow separation, they are quite different near the cell boundaries (figure 13a, c of Kuhlmann *et al.* 1997).

3.2.2. *Different Reynolds numbers, $Re_1 \neq Re_2$*

When $Re_1 \neq Re_2$ the boundary conditions are no longer point symmetric with respect to the centreline $x = y = 0$ and the flow is asymmetric from the outset. Moreover, different basic states must be considered, because the strongly-merged-vortex flow exists only in a certain tongue-shaped region around $Re_1 = Re_2$ (Kuhlmann *et al.* 1997; Albensoeder *et al.* 2001a). Far off-axis ($Re_1 \neq Re_2$) the basic state corresponds to the steady two-dimensional two-vortex flow. This flow, however, is linearly unstable with respect to a long-wavelength mode for increasing $Re_1 + Re_2$ (Kuhlmann *et al.* 1997).

While the four-cell state for $Re_1 = Re_2$ bifurcates out of the quasi-two-dimensional strongly-merged-vortex state, the transition to the cellular states for strongly

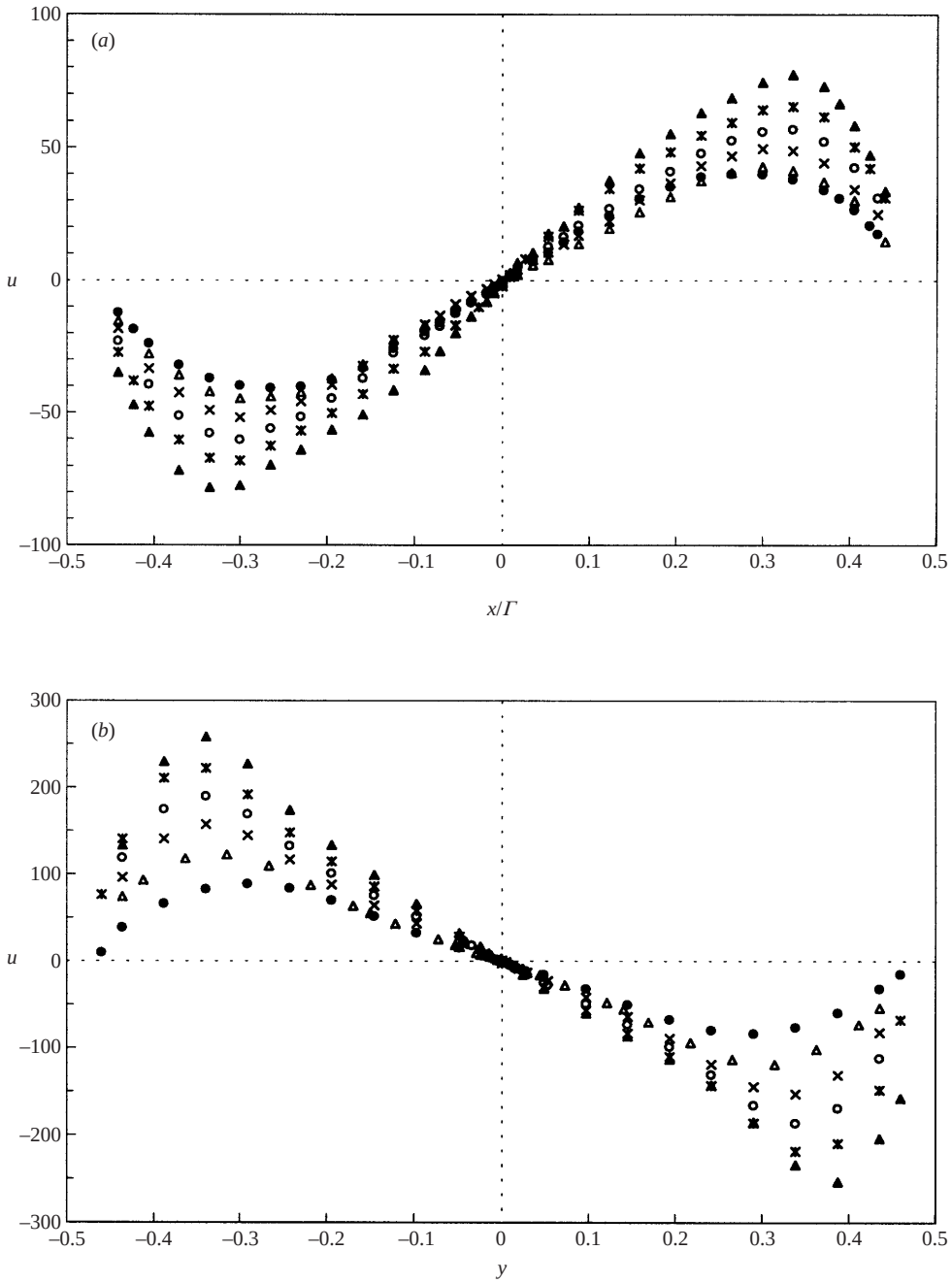

FIGURE 5. Velocity component u in units of v/h measured by LDV within an inner cell of the four-cell V-mode as function of x/Γ (a) and y (b). Data have been taken in the midplane ($z = z_2 = \text{const.} \approx -\Lambda/8$) of the cell. The Reynolds numbers are indicated by symbols: $Re = 300$ (●), 400 (△), 500 (×), 600 (○), 700 (∗), and 800 (▲).

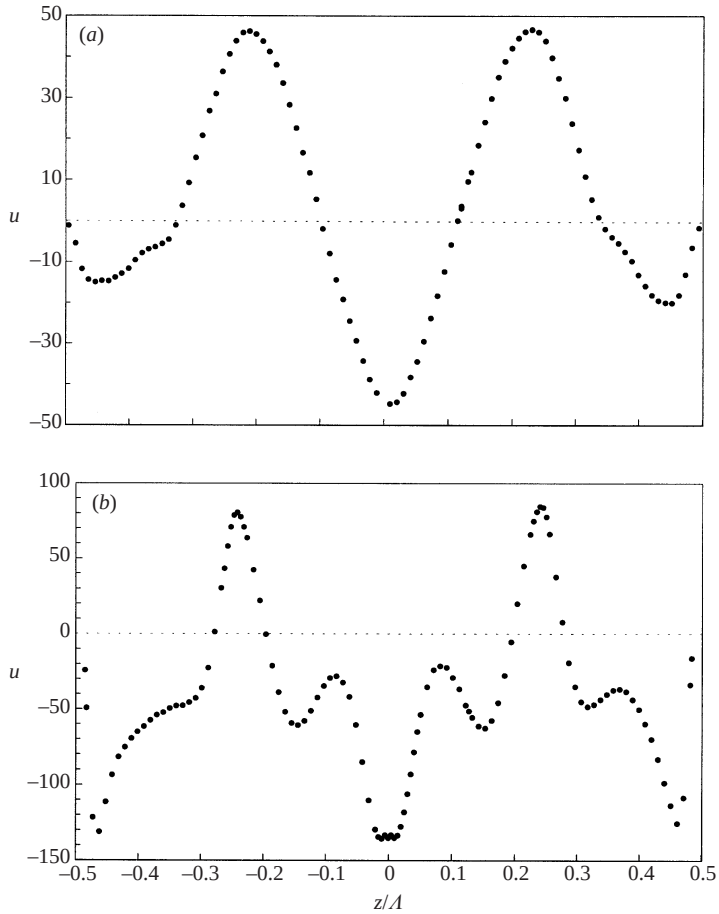

FIGURE 6. LDV measurement of the velocity component u (in units of v/h) as function of z near the centreline for (a) $Re = 325$ and $(x, y) = (0, 0)$ and for (b) $Re = 800$ and $(x, y) = (0, -0.062)$.

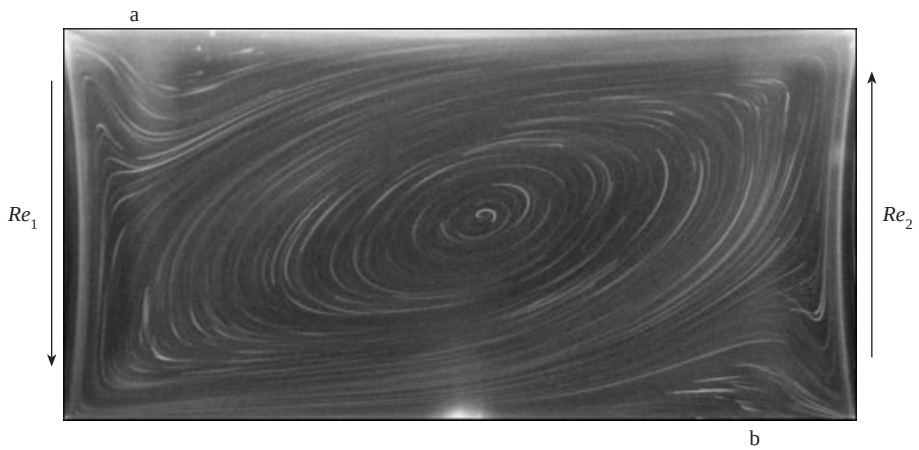

FIGURE 7. Cross-section through the centre of a cell in a four-cell flow at $z \approx \Lambda/8$ for $Re = 800$. Small separated vortices are visible at the top left (a) and the bottom right (b). The arrows indicate the direction of the flow.

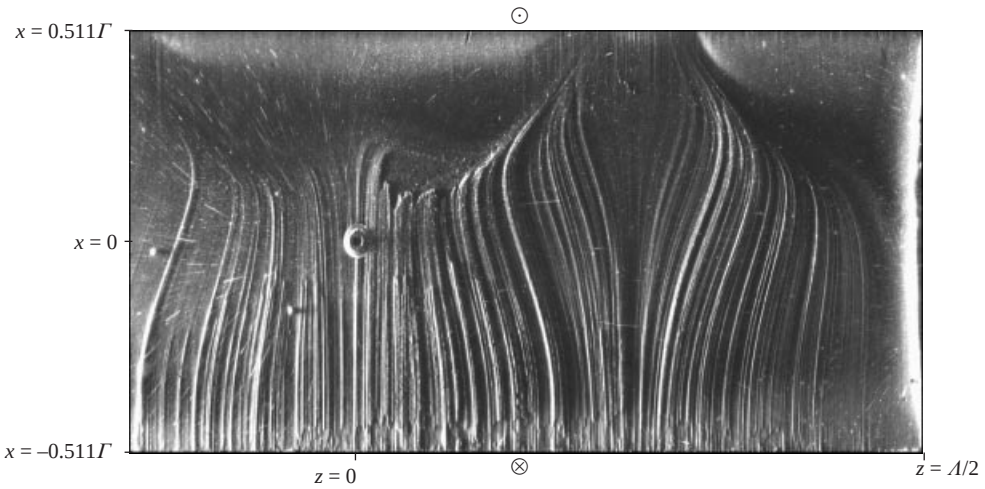

FIGURE 8. Streaks of fine-ground tracer material (aluminium flakes) deposited on the bottom of the cavity which has run continuously for approximately 3 months with a four-cell flow at Reynolds numbers $Re \approx 700$. The streaks on the right-hand side were produced by the end cell. The streaks of the second cell from the right appear in the middle of the figure. On the left, one can see the hot-film probe protruding slightly into the cavity. The upper part of the figure, free of streaks, corresponds to the region of separated flow. The upper and lower boundaries are slightly larger than ± 0.5, since the full bottom plate of size $d_{\max}$ is shown, not only the range corresponding to d. The hot-film probe at $\boldsymbol{x}_b$ had not yet been built-in at the time the photograph was taken.

asymmetric driving, $|Re_1 - Re_2|$ large, is more complicated. However, since the cellular flow develops continuously from the diagonal $Re_1 = Re_2$ when the Reynolds-number difference is increased, and since it can be clearly distinguished from the three-dimensional flow arising as a result of the long-wavelength instability of the two-vortex flow, the existence range of the cellular states can be explored by visual inspection. The measured existence boundaries of the four-cell flow are presented in figure 9 for $Re_1 + Re_2 \leqslant 1400$, extending the range investigated by Kuhlmann *et al.* (1997) who considered $Re_1 + Re_2 \leqslant 870$.

To determine the transition boundaries, a series of experiments has been performed during which one Reynolds number was kept constant and non-zero, while the other was increased quasi-steadily from zero to the bisection $Re_1 = Re_2$. The parameter paths were thus lines parallel to the Reynolds number axes. For $Re_2 > Re_1$ the lines were parallel to the Re_1-axis, and vice versa. The error in Re_i for the existence boundaries of the four-cell modes is estimated to be less than 2% of the Reynolds number that has been kept constant.

When the cells come into existence by increasing Re_1 ($Re_2 = \text{const.}$) the four-cell flow turned out to be of V-type, whereas it was of Λ-type when Re_2 was increased and Re_1 was kept fixed. Since the V- and Λ-modes differ in the bulk only by a translation of $\lambda/2$ in the z-direction, this mode selection is clearly due to the asymmetry of the endwall cells when $Re_1 \neq Re_2$. The pattern selected is such that the apparent vortex cores at $z = \pm\Lambda/2$ always originate near the upstream corner of the fastest moving wall. This behaviour has also been reported by Kuhlmann *et al.* (1997). In the following we discuss the sequence for $Re_2 = \text{const.}$

Within a narrow strip $|Re_1 - Re_2| \lesssim 75$ and as long as the Reynolds number held constant is less than ≈ 290 the increase of Re_1 leads to a jump transition (+ in figure 9, data taken from Kuhlmann *et al.* 1997) from the asymmetric two-vortex

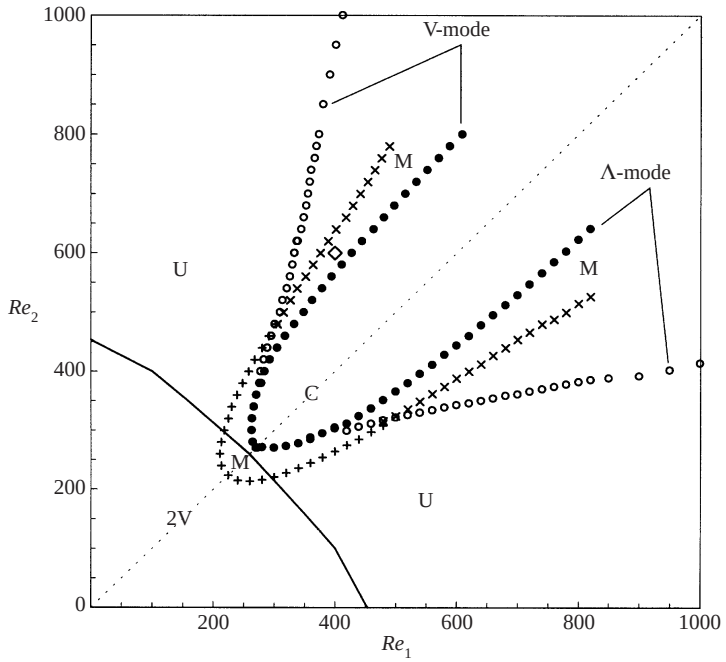

FIGURE 9. Transition boundaries between different flow types in the (Re_1, Re_2)-plane upon a quasi-steady variation of the Reynolds numbers: 2V indicates the region of the two-vortex flow. It becomes unstable to a three-dimensional flow (U). The line is the numerical linear stability boundary of the two-vortex state (Kuhlmann *et al.* 1997). Near $Re_1 = Re_2$ the two-vortex flow changes into the strongly-merged-vortex flow (M). Approaching $Re_1 = Re_2$ from the unstable two-vortex flow (U) the flow first changes into the strongly-merged-vortex flow (M) at the line indicated by + (data taken from Kuhlmann *et al.* 1997) and ×. The unstable two-vortex flow is steady near + and time-dependent near ×. Moreover, the transition to the strongly-merged flow has a small hysteresis (not shown) for +. Thereafter, the strongly-merged flow changes into the four-cell flow (C) at the boundary indicated by ● (V- or Λ-type as indicated). When the path is reversed the four-cell flow breaks down to the unstable two-vortex flow (U) or to the strongly-merged flow (M) at the symbols ○. The diamond ◇ indicates the parameters for figure 10.

flow (2V) to the asymmetric strongly-merged-vortex flow (M). This transition has a small hysteresis (Kuhlmann *et al.* 1997). On a further increase of Re_1 a supercritical transition to a four-cell state occurs, if the curve indicated by ● is crossed near its apex.

When the Reynolds number held constant is larger than ≈ 290 the asymmetric two-vortex flow becomes unstable first to a long-wavelength mode (U) along the line in figure 9 (numerical data of Kuhlmann *et al.* 1997). We did not try to measure this onset, because the critical wavelength $\lambda_c \approx 3.74$ (Kuhlmann *et al.* 1997) is of the order of magnitude of the cavity length Λ and no well-defined critical point exists in the present finite-length apparatus. As long as the constant Reynolds number is not too large (here: $Re_2 < 480$) a jump transition (with a slight hysteresis) from the three-dimensional long-wavelength state (U) occurs at (+) on an increase of Re_1 to the strongly-merged-vortex flow, which is now asymmetric, of course, with respect to the centreline $x = y = 0$. A further increase of Re_1 then leads to an asymmetric four-cell flow (●).

For $Re_2 \gtrsim 480$, the three-dimensional long-wavelength state becomes time-dependent for sufficiently high Re_1. A further increase of Re_1 then leads to a transition from this

time-dependent flow (also denoted by U) to the steady asymmetric strongly-merged-vortex flow (M), the transition boundary being indicated by $\times$ in figure 9. Within the experimental accuracy this transition shows no hysteresis. The subsequent transition from the strongly-merged-vortex flow (M) to the cellular state ($\bullet$) is found to be discontinuous and the cellular state comes into existence with a finite amplitude.

When the Reynolds-number difference is small, the three-dimensional cellular state has a small amplitude at the threshold. In the limit $Re_1 = Re_2$ the bifurcation from the strongly-merged-vortex state is supercritical (see e.g. figure 3). For larger Reynolds number differences, we find a hysteresis and the bifurcation is subcritical. This can be seen from the deviation between $\bullet$ and $\circ$ in figure 9. The latter symbols indicate the breakdown of the four-cell pattern upon a decrease of one Reynolds number (keeping the other one constant). For $Re_2 \gtrsim 400$, for example, the hysteresis of the transition to and from the four-cell V-mode increases considerably with Re_2 (figure 9), consistent with Kuhlmann *et al.* (1997).

Owing to the strong selection of the pattern (V or Λ) by the asymmetric endwall cells, the domain of existence of a particular pattern (e.g. V) is not symmetric with respect to the diagonal $Re_1 = Re_2$. Here we have measured the existence range of the preferred pattern. When the increasing Reynolds number crosses the bisection $Re_1 = Re_2$ the previously preferred mode becomes the non-preferred one and, on a further increase of the Reynolds number, it will suffer an earlier breakdown than the preferred mode. We have not yet investigated the upper existence boundaries of these non-preferred modes.

An example of the asymmetric strongly-merged-vortex flow (M) is shown in figure 10 for $(Re_1,Re_2)=(400,600)$; the location in the (Re_1, Re_2)-plane is indicated by a diamond ($\diamond$) in figure 9. The flow consists of two primary vortices adjacent to both moving walls embedded in a globw al recirculation. The primary vortex adjacent to the slower moving wall (left) is much weaker than the one next to the faster moving wall (right). Due to the weaker suction of the upstream corner of the slower moving wall a secondary separated vortex is established in the flow approaching the upstream corner of the slower moving wall (top left of figure 10). A comparison of the experimental streaklines with the numerically calculated stream function of the asymmetric strongly-merged-vortex flow is shown in figure 10(*b*). The slight difference in the streakline patterns is attributed to three-dimensional finite-size effects for $\Lambda = 6.55$ which appear to be more significant for asymmetric driving than for $Re_1 = Re_2$.

3.3. *Five-cell flow*

Besides the four-cell flow, we also found a flow comprising five cells in the spanwise direction. It is observable only within the existence range of the four-cell flows. The five-cell flows have essentially the same properties as the four-cell flows, except that the somewhat *higher* existence boundaries indicate that the flow with a shorter wavelength corresponding to five cells is not as preferred as the four-cell flow. Even though a five-cell flow would be the preferred state according to the neutral curve (cf. figure 7 of Kuhlmann *et al.* 1997) if the cell size were homogeneous, we find that the four-cell flow has a lower threshold. This could be a consequence of the size of the cells adjacent to the endwalls, which are rather large in the four-cell flow. Therefore, the effective wavenumber of the innermost cells of the four-cell flow is larger than expected on pure geometrical grounds.

The five-cell flows could only be realized by particular initial and transient conditions for the wall speeds. For instance, the five-cell V-mode was set up by increasing both Reynolds numbers from rest to $Re_1 = Re_2 = 450$ by a fast linear ramp

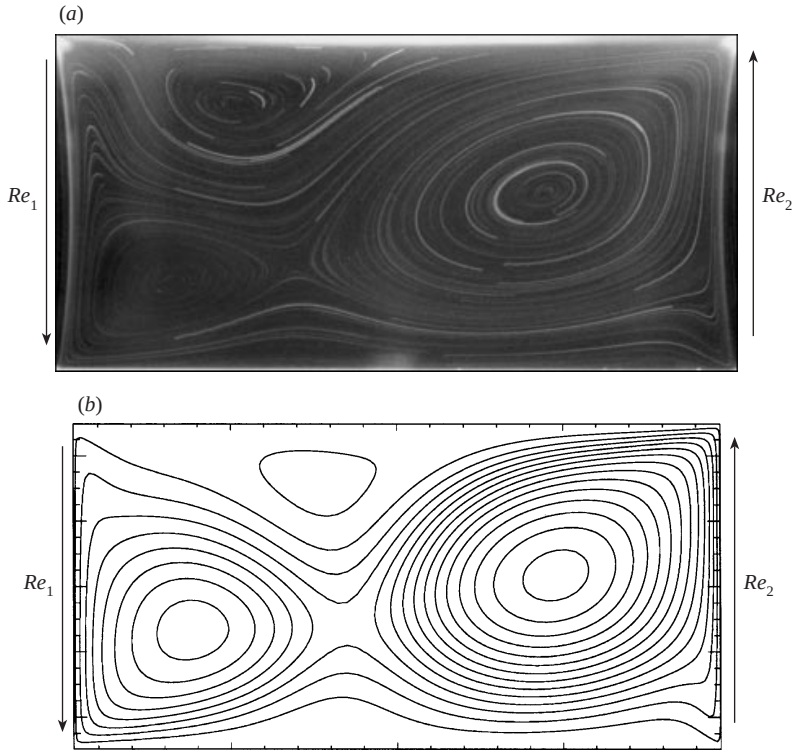

FIGURE 10. Streaklines of the strongly merged-vortex flow in the (x, y)-plane at $z = 0$ (a) and numerically calculated streamlines of the two-dimensional strongly-merged-vortex flow (b) using the code of Albensoeder *et al.* (2001*a*), both for $Re_1 = 400$ and $Re_2 = 600$. The arrows indicate the direction of the lid motion.

$\mathrm{d}Re/\mathrm{d}t \approx 100\ \mathrm{s}^{-1}$ corresponding to a dimensionless rate $r_i \approx 3788$. On the other hand, the five-cell Λ-mode was obtained from a four-cell V-flow at $Re = Re_1 = Re_2 = 500$ as follows. First, Re_1 was rapidly reduced to $Re_1 = 330$ at a rate $\mathrm{d}Re/\mathrm{d}t \approx -100\ \mathrm{s}^{-1}$ ($r_1 \approx -3788$) keeping $Re_2 = 500$ constant. After a few seconds the four cells started to move in the positive z-direction. As a result, the cell adjacent to the stationary wall at $z = -\Lambda/2$ became slightly larger. By increasing Re_1 again up to $Re_1 = 500$ with $\mathrm{d}Re_1/\mathrm{d}t \approx 100\ \mathrm{s}^{-1}$ a fifth cell was created next to the stationary end wall at $z = -\Lambda/2$ and a persistent stationary five-cell Λ-mode was established. The difference in the procedures to create the V- and Λ-type of flows indicates the role of even slight imperfections in the experimental setup.

3.3.1. *Equal Reynolds numbers, $Re = Re_1 = Re_2$*

The dependence of the velocity component u measured by LDV at $(x, y) = (0, 0.183)$ for a five-cell V-mode as function of the spanwise coordinate z is shown in figure 11 for $Re = 850$. The structure of the three interior cells appears to be hardly influenced by the end effects. Their size corresponds to a wavenumber $k = 2.44 \pm 0.05$. The above-mentioned mirror symmetry with respect to the cell boundaries at $z = \pm 0.1\Lambda$ is clearly visible. Likewise, the flow within each individual interior cell of the five-cell pattern is point symmetric. The change of sign of the velocity near the cell boundaries at $z = -0.3\Lambda$ and $z = 0.1\Lambda$ is due to the squeezing of the recirculating flow in the (x, y)-plane to a thin shear layer near the top lid at $y = 1/2$ (see figure 13 in Kuhlmann

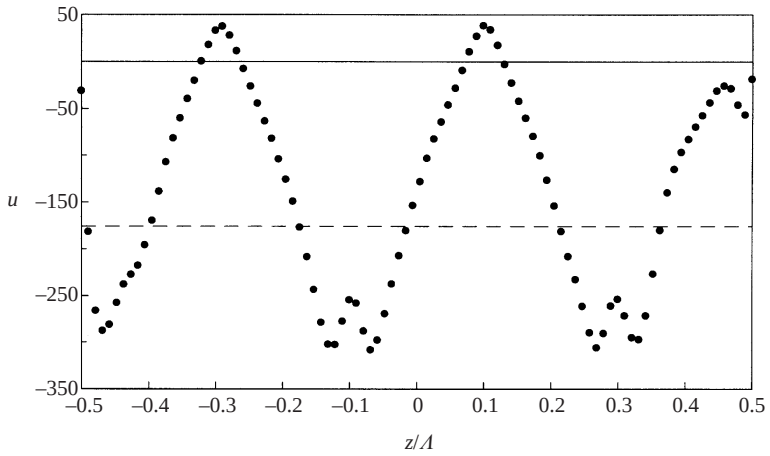

FIGURE 11. Velocity component u in units of v/h as function of z at $(x, y) = (0, 0.183)$ for the five-cell V-mode at $Re = 850$. The dashed line indicates the unperturbed velocity value $u = -176$ of the unstable two-dimensional solution of the infinite system calculated with the code of Albensoeder *et al.* (2001*a*). The full line is $u = 0$.

et al. 1997): when the measuring location z enters this region a flow reversal is seen. In a similar way, the decrease in the amplitude at $z = -0.1\Lambda$ and $z = 0.3\Lambda$ can be explained in terms of the cellular flow structure.

The cells adjacent to each rigid boundary at $z/\Lambda = \pm 0.5$ are only weakly disturbed. Most notably, the amplitude (deviation from the two-dimensional-flow value, dashed in figure 11) of the three-dimensional flow close to the stationary sidewalls is not as high as it is near the interior cell boundaries. The size of the cells at this Reynolds number is even less influenced: the endwall cells are only 5% larger (in the z-direction) than the inner cells.

The spatial structure of the cellular flow has been measured on a three-dimensional grid using LDV. Owing to the symmetry of the flow it is sufficient to show only the upper half of a single cell. The projections of the velocity vectors of the second cell centred at $\boldsymbol{x}_2 = (x_2, y_2, z_2) = (0, 0, -0.195\Lambda)$ of a five-cell V-mode at $Re = 700$ (see figure 2*c*) onto three horizontal planes at $y = 0.048$ (near the centre), $y = 0.242$ (intermediate), and $y = 0.387$ (near the top wall) are shown in figure 12(*a–c*).

Near the midplane $y \approx 0$ (figure 12*a*) the point symmetry of the velocity field is visible. Closer to the upper stationary wall (figure 12*b, c*) the projected velocity is directed approximately diagonally across the cell. This is consistent with the streaklines shown in figure 2. Next to the upper wall the flow is dominated by the two-dimensional flow components u and v, whereas w is small. An indication for the flow separation mentioned above (figures 7 and 8) for the four-cell flow is also visible in figure 12(*c*). In the lower part of this figure the fluid is strongly decelerated, after crossing the diagonal, and the flow changes its direction from the positive to negative z-direction.

3.3.2. *Different Reynolds numbers, $Re_1 \neq Re_2$*

When the Reynolds numbers are reduced the five-cell flows cease to exist. When the transition point is approached the amplitude of the five-cell flow does not continuously go to zero. Rather, it breaks down suddenly from a flow state with finite amplitude. Therefore, their existence ranges, measured for $Re_{1,2} \leqslant 1100$, are easily detectable. Results for the five-cell Λ-mode are shown in figure 13 where the plusses (+) indicate

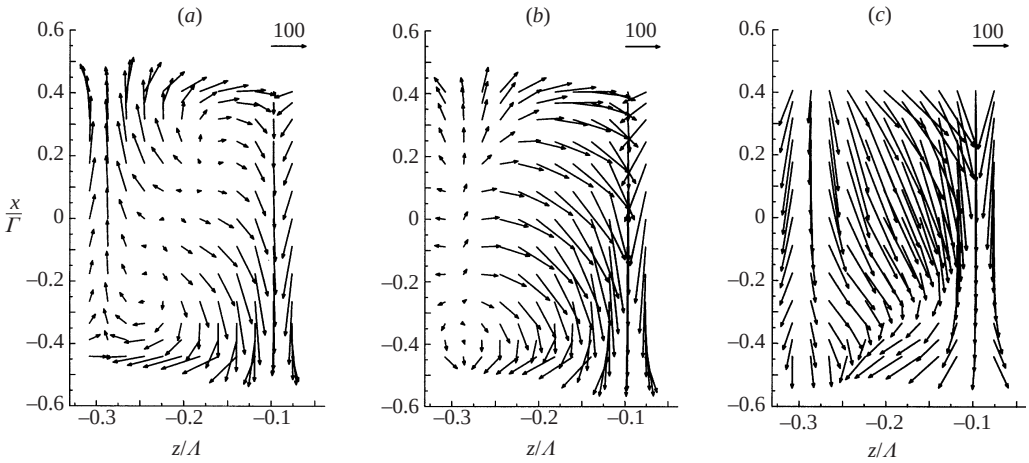

FIGURE 12. Projections of the steady velocity field of the five-cell flow for $Re = 700$ onto planes $y = 0.048$ (a), $y = 0.242$ (b), and $y = 0.387$ (c). The length of the arrow in the upper right corners specifies the velocity scale $w = 100$ (in units of v/h).

the breakdown of the five-cell Λ-mode when the Reynolds number Re_2 is decreased from the diagonal $Re_1 = Re_2$ by keeping Re_1 fixed, or vice versa. The squares (■) indicate the breakdown of the five-cell V-mode. For comparison, the existence boundaries of the four-cell modes from figure 9 are included. Because the five-cell modes are antisymmetric with respect to $z = 0$, the V-mode is the mirror image of the Λ-mode, and the existence ranges of both modes should coincide. In fact, we find that both five-cell states break down at approximately the same Reynolds numbers, differing at most by 4% of the Reynolds number that has been kept constant. The systematic deviation – the V-mode (■) breaks down at slightly lower Re_1 than the Λ-mode (+) is attributed to small experimental imperfections, in particular at the endwalls ($z = \pm\Lambda/2$), because these strongly select the pattern (see § 3.2.1 above).

The breakdown curves of the five- and the four-cell patterns become very close to each other locally and even intersect (figure 13). If $Re_1 > Re_2$ the five-cell Λ-mode, for which most measurements have been made, undergoes a transition to a four-cell Λ-flow for $Re_1 \leqslant 600$. For $650 \leqslant Re_1 \leqslant 1000$ the five-cell states break down to the three-dimensional long-wavelength state mentioned above, and at higher Reynolds numbers, $1050 \leqslant Re_1 \leqslant 1100$, the transition is again to the four-cell Λ-mode.

When $Re_2 > Re_1$, the five-cell Λ-mode develops into a four-cell V-mode upon a decrease of Re_1 as long as $Re_2 \leqslant 450$. In the range $500 \leqslant Re_2 \leqslant 750$ the five-cell Λ-mode changes to a five-cell V-mode which then decays to the three-dimensional long-wavelength flow pattern (■ in figure 13). At even higher Reynolds numbers, $Re_2 \geqslant 800$, the five-cell Λ-flow directly decays to the three-dimensional long-wavelength flow, although a four-cell flow exists there, too, in a very narrow range of Re_1. On the other hand, the five-cell V-mode (■) develops into a four-cell V-mode for $Re_2 \leqslant 500$ on a decrease of Re_1. For higher Re_2 it decays to the three-dimensional long-wavelength flow.

Finally, on a decrease of the Reynolds numbers along the diagonal $Re_1 = Re_2$, both the five-cell Λ-mode and the five-cell V-mode break down to the four-cell V-mode which seems to be the preferred mode in our apparatus (see figure 3) at $Re = 346$ and $Re = 344$, respectively.

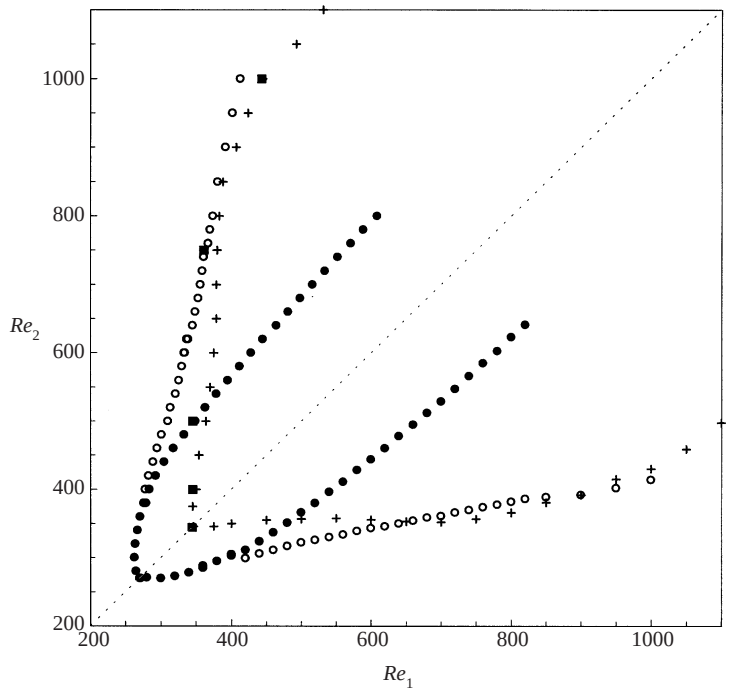

FIGURE 13. Existence range of the V- (■) and the Λ- (+) five-cell flows in the (Re_1, Re_2)-plane. The existence boundaries agree within 4% of the maximum Reynolds number $\max\{Re_1, Re_2\}$. Data marked as ● and ○ indicate the existence boundaries of the four-cell V- and Λ-modes from figure 9.

4. Time-dependent three-dimensional flows

The stationary cellular flows are very robust. However, if the Reynolds numbers are further increased in a quasi-steady manner as described in § 3.2, a secondary instability is encountered at which the cellular flow becomes time-dependent. During the transition to a time-dependent flow, the individual cells remain clearly distinct and the number of cells does not change.

As long as the amplitudes of oscillation of the wall shear stress are small the response curves of the hot-film probes can be linearized. Then the hot-film measurements allow the determination of the frequency spectrum. To that end 2^{16} data points have been measured with a sampling rate of $f_s = 500\,\mathrm{Hz}$ for every parameter set (Re_1, Re_2). The spectral components could thus be determined up to $f_{\max} = 250\,\mathrm{Hz}$. No relevant frequencies were found, however, beyond $f > 10\,\mathrm{Hz}$. Therefore, the spectrum was only calculated up to $f_{\max} = 10\,\mathrm{Hz}$ by Fourier analysis. The crucial condition of a small amplitude of the shear-stress oscillations is satisfied here, because the oscillatory instability was found to be supercritical within small error bounds, unless noted otherwise. In all cases, quantitative LDV measurements confirmed the hot-film measurements.

For the following discussion it is useful to represent any function $g(\boldsymbol{x}, t) \in [u, v, w, p, A]$ which is periodic in time with period $f_1^{-1} = 2\pi/\omega_1$ as

$$g(\boldsymbol{x}, t) = \frac{1}{2} \sum_{n=0}^{\infty} g_n(\boldsymbol{x})\, \mathrm{e}^{\mathrm{i}(n\omega_1 t + \varphi_n)} + \text{c.c.} \tag{4.1}$$

Here g_n denotes the real amplitudes of the spectral components of g with frequencies

$\omega_n = n\omega_1$ which are integer multiples of the fundamental frequency ω_1. The absolute value of the shear stress measured by a hot-film probe at $\boldsymbol{x}_i$, $i \in \{a, b\}$, is denoted as $A(\boldsymbol{x}_i, t) = \rho\nu|\partial_y \boldsymbol{u}(\boldsymbol{x}, t)|_{x=x_i}$. Since only the absolute value of the shear stress can be measured, the sign remains undetermined. However, the steady shear-stress component A_0 is dominant. Therefore, flow fluctuations parallel to the mean flow can be analysed exactly. This does not apply to the velocity fluctuations perpendicular to the mean flow and the measurements must be interpreted with care.

4.1. *Equal Reynolds numbers, $Re = Re_1 = Re_2$*

When the Reynolds number is increased rapidly above the critical value $Re_c^{(2)}$ the oscillations of the individual cells are not synchronized at first. After a certain period of time, however, or during a quasi-steady increase of Re, the cells become synchronized and the oscillations appear as standing waves (cf. figure 19 below) with the same wavelength as the underlying cellular flow. Since the oscillatory flow arises from a steady three-dimensional flow state, the linear instability mode is harmonic in time but not harmonic in space. Near the threshold, only the spectral component of the flow field with the fundamental frequency ω_1 is of sizeable magnitude. Three instants during one period of oscillation are shown in figure 14. For symmetrical driving, the oscillatory flow within each cell remains point symmetric with respect to the centre of that cell at any time. It is observed that jets approaching the moving walls form between adjacent cells (arrows in figure 14). These jets oscillate in the z-direction with the fundamental frequency ω_1. All jets approaching the same moving wall oscillate in phase. The jets approaching the other moving wall are out of phase by π. It follows that the velocity component w_1 of the fundamental oscillatory mode has antinodes at the mean locations of the cell boundaries. From continuity we conclude that the components u_1 and v_1 must have nodes at the cell boundaries. Therefore, w_1 is symmetric and u_1 and v_1 are antisymmetric with respect to the steady-state locations of the cell boundaries. Because w_1 does not vanish on the cell boundaries, the cells undergo shape oscillations around their steady-state positions. During these oscillations the cells change their shape and alternatingly grow and shrink in width (z-direction). This behaviour can be seen from figure 14.

Examples of typical frequency spectra are shown in figure 15 at $Re = 860$. The data have been measured by the hot-film probes at $\boldsymbol{x}_a$ and $\boldsymbol{x}_b$ which approximately lie respectively on a cell centre and a cell boundary in the oscillatory four-cell V-mode. The dominance of the fundamental $f_1 = 1.495\,\mathrm{Hz}$ in figure 15(a) indicates weakly nonlinear oscillations. On the cell boundary (figure 15b), however, A_1 is very small compared to the amplitude of the second harmonic A_2, indicating a node of A_1 at the bottom centre ($x = 0$) of the cell boundary. The amplitude A_1 does not exactly vanish in figure 15(b), because the actual cell boundary (determined by LDV) is not exactly located above the (fixed) hot-film probe. This behaviour is consistent with the symmetries of the fluctuating velocity components. The steady-state (mean) components u_0 and v_0 must have a local extremum on the cell boundary (jets indicated in figure 14), because they are symmetric with respect to it (w_0 is antisymmetric). The only non-zero fundamental-frequency component at the mean location of the cell boundary is w_1. It causes a small-amplitude oscillation in the z-direction with frequency f_1 of the local extremum of, for example, u. For such a total-flow oscillation, the fundamental frequency f_1 cannot be measured at the mean location of the cell boundary, merely the second harmonic u_2 with frequency $f_2 = 2f_1$ and, of course, w_1 can be measured there. The frequency of the shear stress due to w_1 measured by the hot-film probe, however, is f_2, since only the absolute value can be measured and

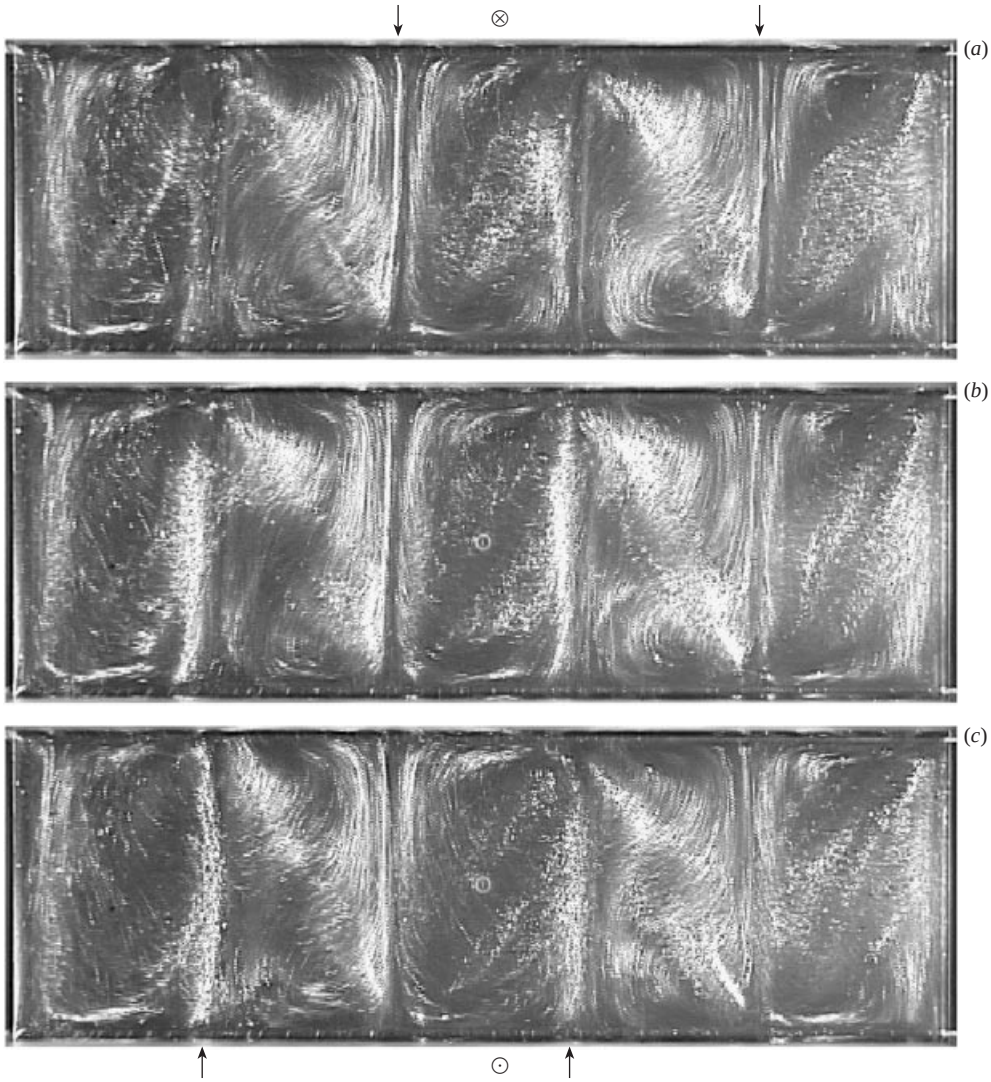

FIGURE 14. Visualization with aluminium flakes of the oscillatory five-cell Λ-flow at $y = 0$ for $Re = 900$ at three instants during one period T of oscillation: $t = 0$ (*a*), $t = 4T/15$ (*b*), and $t = 8T/15$ (*c*). Note the slight changes in shape and width (in the z-direction) of the interior cells. The arrows indicate the locations of the jets approaching the moving walls. The jets approaching the lower moving wall in the figure are harder to see than those approaching the upper moving wall, because of the non-isotropic visualization with aluminium flakes. The direction of wall motion is indicated by ⊙ and ⊗.

w_1 fluctuates around zero. Moreover, the amplitude u_2 is quadratically small there (compared to the components u_1, v_1 and w_1).

Both LDV and hot-film measurements confirm that the oscillatory instability is supercritical and of *tricritical* type, i.e. the amplitude of the fundamental Fourier component f_1 increases with the fourth root of the distance from the critical point. The term *tricritical* was introduced for non-equilibrium phenomena by Steinberg & Brand (1984) who took the name from the tricritical point in phase transitions. The tricritical character of the bifurcation is demonstrated in figure 16 where the

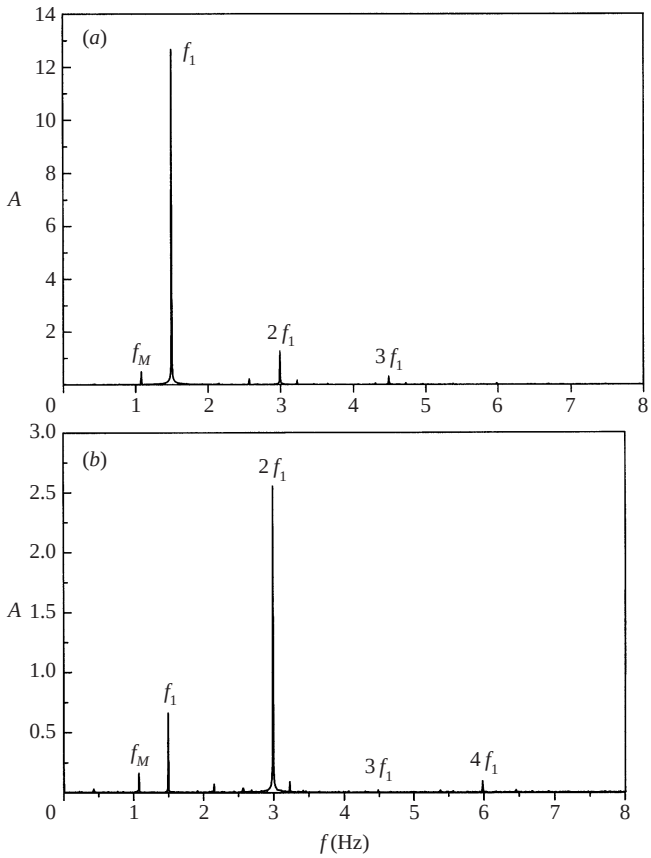

FIGURE 15. Shear-stress frequency spectra of the four-cell V-mode at $Re = 860$. Data were obtained by hot-film probes flush mounted to the bottom plate at $\boldsymbol{x}_b = (0, -1/2, \Lambda/8)$ near a cell centre (a) and at $\boldsymbol{x}_a = (0, -1/2, 0)$ near a cell boundary (b). The motor frequencies are denoted f_M. Note the different scales of the shear-stress amplitudes A which are plotted in arbitrary units.

fourth power of the fundamental shear-stress amplitude is plotted as a function of the Reynolds number. The intersection point of the linear extrapolation with the Reynolds-number axis yields $Re_c^{(2)} = 825 \pm 1.5\%$ for both the V- and the Λ-modes. The dependence of the dimensionless oscillation frequency on Re is shown in figure 17. The critical frequency is $f_c = 1.437\,\mathrm{Hz}$ corresponding to a dimensionless value $F_c = f_c h^2/\nu = 62.0$. The frequency increases slightly on an increase of the Reynolds number. Up to $Re = 1200$ no incommensurate frequencies were found.

The time-dependent bifurcations of the five-cell flows are qualitatively the same as those of the four-cell flows. Both steady five-cell flows become unstable at $Re_c^{(2)} = 875 \pm 1.5\%$. The dependence of the amplitude of the fundamental Fourier component u_1, measured by LDV, on the Reynolds number is shown in figure 18. In the particular experimental run shown, the flow bifurcates at $Re_c^{(2)} = 880$. The linear dependence of u_1^4 on $\epsilon = (Re - Re_c^{(2)})/Re_c^{(2)}$ up to $Re = 950$ confirms the tricritical character of the instability. The dimensionless frequency at onset is $F_c = 62.0$, as for the four-cell flows.

The amplitudes of u_1 have been measured by LDV for $Re = 880$ in a five-cell V-mode about 1% above the critical Reynolds number for the onset of oscillation ($Re_c^{(2)} = 872$). The dimensionless fundamental frequency is $F_1 = 61.6 \pm 0.1$. The data

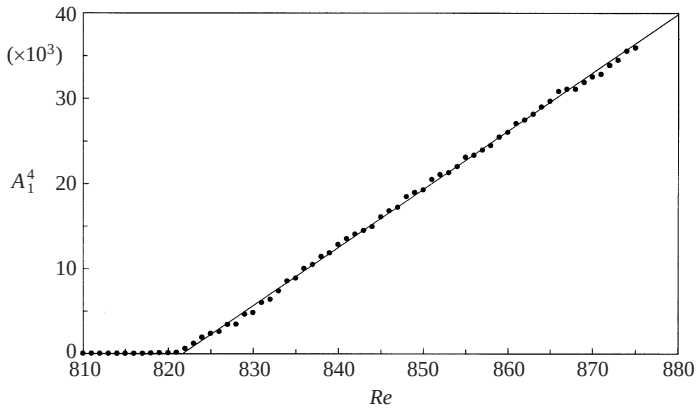

FIGURE 16. Fourth power of the shear-stress amplitude A_1 (arbitrary units) measured by the hot-film probe in a four-cell V-flow at $\boldsymbol{x}_b = (0, -1/2, \Lambda/8)$ (middle of a cell) as function of the Reynolds number Re. The critical Reynolds number is $Re_c^{(2)} = 821$. The line is a least-squares fit.

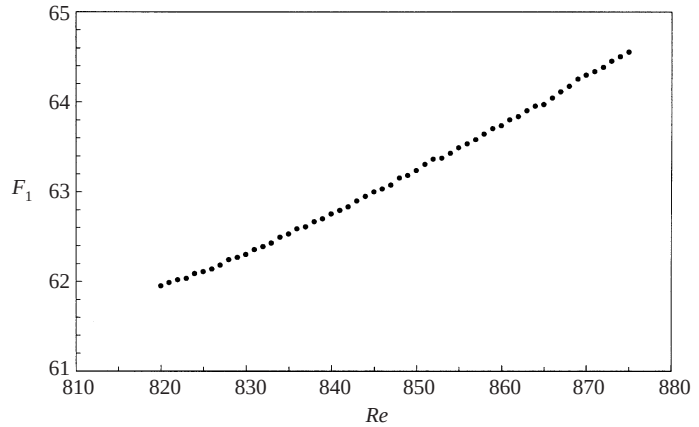

FIGURE 17. Fundamental frequency F_1 of the oscillatory four-cell V-mode in units of ν/h^2 as a function of the Reynolds number. The data were obtained by the hot-film probe at $\boldsymbol{x}_b = (0, -1/2, \Lambda/8)$.

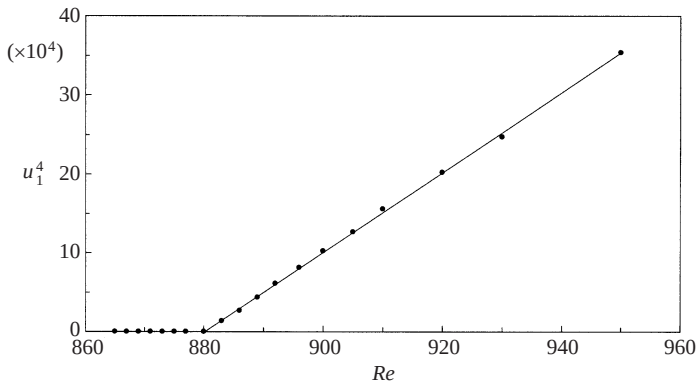

FIGURE 18. Fourth power of u_1 (in units of ν/h) measured by LDV at $\boldsymbol{x} = (0, 1/4, 0)$ (above the centre of the middle cell) in a five-cell V-flow as function of the Reynolds number Re.

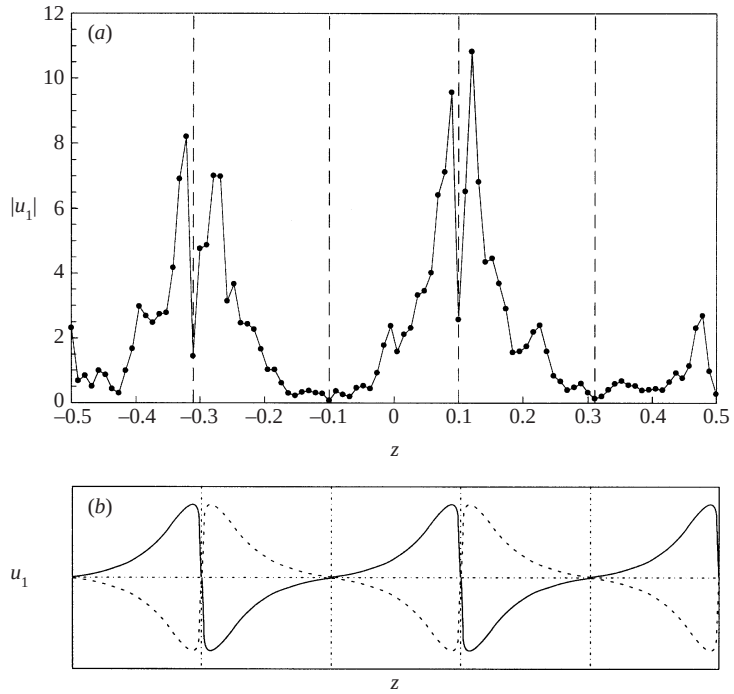

FIGURE 19. (*a*) LDV measurements of the amplitude u_1 in units of v/h as function of the spanwise coordinate z for $Re = 880$ ($\epsilon = 0.01, F_1 = 61.6 \pm 0.1$) at $(x, y) = (0, 1/4)$ for a five-cell V-mode. (*b*) Sketch of the standing wave of u_1 corresponding to (*a*). The two instants of maximum absolute velocity are shown.

were taken at $(x, y) = (0, 1/4)$ using spanwise steps of $\Delta z = 2\,\mathrm{mm}$ corresponding to $\Delta z/\Lambda \approx 0.01$. Figure 19(*a*) shows $u_1(0, 1/4, z)$ as function of z. The component u_1 has nodes at the boundaries of the cells at $z/\Lambda = \pm 0.31 \pm 0.006$ and $z/\Lambda = \pm 0.1 \pm 0.006$, as well as on the stationary sidewalls ($z/\Lambda = \pm 1/2$). The vertical dashed lines in figure 19(*a*) indicate the steady-state locations of the cell boundaries at which the phase of u_1 jumps by π (standing wave) as sketched in figure 19(*b*). The z-dependence of the underlying steady-state cellular flow is clearly reflected by the strong non-harmonic character in z of the amplitude u_1. Since the data were not taken on the centreline $x = y = 0$, the oscillation amplitudes u_1 are not symmetrical in z with respect to the centres of the cells z_n, $n \in [1, 2, 3, 4, 5]$. The oscillatory amplitude u_1 is large near $z/\Lambda \approx -0.31$ and $z/\Lambda \approx 0.1$, because the measuring locations are in a region where the basic flow exhibits high gradients $|\partial_y u|$ (see figure 13 of Kuhlmann *et al.* 1997) and in which small fluctuations of v result in large fluctuations of u. The strong vertical (y) gradient of u at $z/\Lambda = -0.3$ is also visible in figures 12(*a–c*) where the steady velocity field of the same flow type (five-cell Λ-type) is shown: the velocity u at the left-hand cell boundary changes its sign (strong shearing) as function of y. Conversely, the measuring locations near $z/\Lambda \approx -0.1$ and $z/\Lambda \approx 0.31$ in figure 19(*a*) are in a region of weak basic-state flow gradients. Hence, the oscillations are comparatively weak there.

4.2. *Different Reynolds numbers:* $Re_1 \neq Re_2$

The critical point $Re_c^{(2)} = Re_{1,c}^{(2)} = Re_{2,c}^{(2)}$ extends to a critical curve for the onset of oscillation in the (Re_1, Re_2)-plane. For an investigation of the bifurcation to oscillations

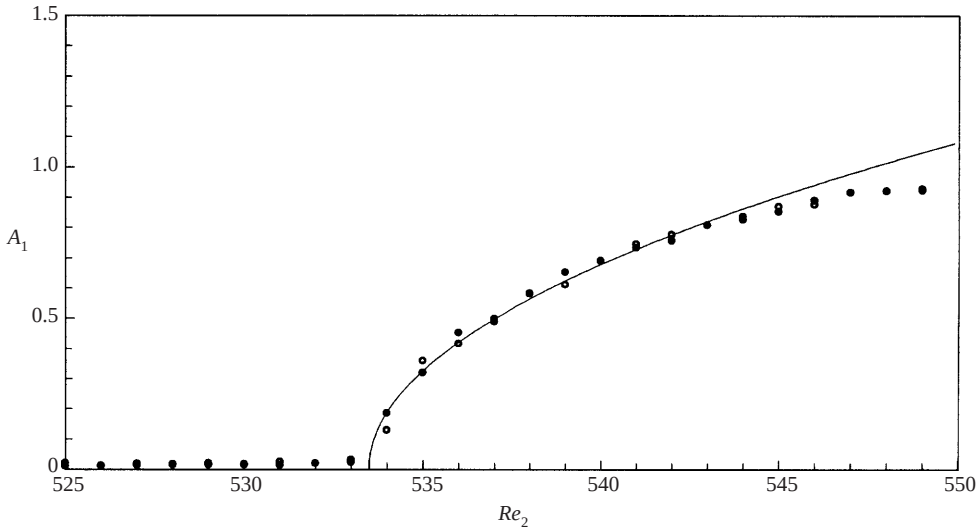

FIGURE 20. Shear-stress amplitudes of oscillation A_1 (arbitrary units) of the fundamental frequency f_1 of a four-cell Λ-mode measured by the hot-film probe at $\boldsymbol{x}_a = (0, -1/2, 0)$ for $Re_1 = 900$ as function of Re_2 during an increase (●) and during a decrease (○) of Re_2. The solid curve is a fit $A_1 \sim \sqrt{\epsilon}$ yielding the bifurcation point $(Re_{1,c}, Re_{2,c}) = (900, 533.5)$. Note that the measurement location does not correspond to the exact position of the cell boundary between the two innermost cells. Since the the maximum Fourier amplitude in the range $1.40 \leqslant f\,[\mathrm{Hz}] \leqslant 1.45$ has been plotted, the (positive) subcritical data points represent a measure of the noise level.

for $Re_1 \neq Re_2$, the oscillating amplitudes can be measured along any straight line crossing the critical curve. Note that the exponent of the asymptotic power law (for $(Re_1, Re_2) \to (Re_{1,c}^{(2)}, Re_{2,c}^{(2)})$) for the dependence of the amplitude on the distance from the critical point does not depend on the angle under which the critical curve is crossed. A tricritical bifurcation, however, is only found at the point $Re_{1,c}^{(2)} = Re_{2,c}^{(2)}$ on the diagonal.

As an example of an off-diagonal bifurcation, we show in figure 20 the amplitude of the fundamental shear-stress component A_1 as a function of Re_2, keeping Re_1 constant at $Re_1 = 900$. Every data point was measured after having increased (●) or decreased (○) the Reynolds number Re_2 by $\Delta Re_2 = 1$ and waiting for 30 minutes, roughly corresponding to the momentum diffusion time τ_l in the spanwise direction. The error in the amplitude is estimated to be less than 5%, except extremely close to the threshold. The critical point is $(Re_1, Re_2) = (900, 533.5)$. Since the z-location of the cell boundary differs slightly from the z-location of the hot-film probe, and owing to the large slope (with respect to z) of the fundamental Fourier component at the cell boundary (see figure 19), a small-amplitude signal A_1 can be measured, even though it must vanish exactly on the cell boundary (w_1 does not contribute to A_1 on a cell boundary). From figure 20 we find a dependence $A_1 \sim \epsilon^{1/2}$, where $\epsilon = (Re_2 - Re_{2,c}^{(2)})/Re_{2,c}^{(2)}$. The solid curve in figure 20 is a fit $A_1 = \beta\epsilon^{1/2}$ with $\beta = 0.2665$.

The critical curves for the onset of time-dependence in the four-cell and five-cell flows are shown in figure 21. For completeness the figure also shows the existence ranges of the steady cellular flows. The critical Reynolds numbers were determined in a similar way as the existence ranges of the stationary cellular flows by keeping one Reynolds number constant and varying the other one. More specifically, for the four-cell flow Re_1 was varied for constant $Re_2 \in [550, 820]$ $(Re_1 > Re_2)$ and for

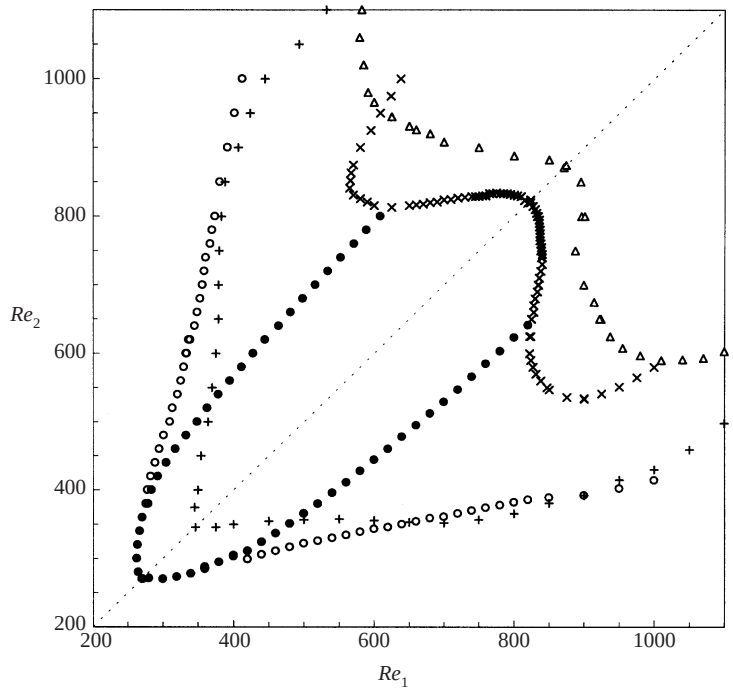

FIGURE 21. Critical curves for the onset of the time-dependent four- (×) and five-cell flows (△) and existence ranges of the steady four- (○,●) and five-cell flows (+) as in figure 13.

$Re_2 \in [852, 1000]$ ($Re_1 < Re_2$). The remaining points and those for the five-cell flows were determined in a similar way. We found that the critical curves for the V- and Λ-modes coincide for both four- and five-cell flows with an error less than 3% of the largest of the two critical Reynolds numbers.

Close to the parameter region where the onset curve for time-dependent four-cell flow (×) intersects the onset curve for the steady four-cell flow (●) ($560 \leqslant Re_j \leqslant 650$), we observed that the oscillation amplitude, on an increase of Re_i ($i \neq j$), jumps from zero in the steady four-cell flow to a finite value at the critical point, the oscillatory amplitude remaining nearly independent of Re_i near the bifurcation point. By decreasing Re_i again, the time-dependent flow jumps back (within the error bounds of the critical values) at the same critical point to the steady four-cell flow, without hysteresis. The origin of this behaviour is as yet unknown.

5. Summary and concluding remarks

Steady and time-dependent flows in a two-sided lid-driven cavity with cross-sectional aspect ratio $\Gamma = 1.96$ have been investigated experimentally. The two steady and well-separated vortices that exist for low Reynolds numbers merge to a highly strained vortex when both sidewall Reynolds numbers are simultaneously increased from zero. For Re slightly larger than this quasi-two-dimensional transition Reynolds number the strained vortex undergoes a bifurcation to a steady cellular flow, caused by the elliptic instability mechanism. The bifurcation to steady cells is a standard supercritical pitchfork bifurcation. In the present experiment with spanwise aspect ratio $\Lambda = 6.55$ the supercritical flow consists of four cells corresponding to two wavelengths. Five-cell flows were also accessible by particular transient conditions. A

flow with six cells in the spanwise direction has been observed, but no qualitative and quantitative investigations were carried out.

For equal Reynolds numbers the flow within each single cell (apart from those next to the endwalls) is point symmetric, to a good approximation, with respect to the centre of the cell. On a further increase of the Reynolds numbers standing waves set in. They have the same fundamental wavenumber as the steady cellular flow and the oscillatory flow is also point symmetric, at any instant of time, with respect to the centre of each cell. The oscillatory flow bifurcates from the steady cells via a tricritical bifurcation for which the amplitude of oscillation increases with the fourth root of the distance from the critical point. Up to $Re = 1200$ no evidence for further incommensurate frequencies was found.

When both Reynolds numbers differ from each other the point symmetry of the cellular flow is lost, yet the steady cells remain rectangular. The bifurcation to oscillations, however, is no longer tricritical and the oscillation amplitude of the fundamental Fourier component increases with the square root of the distance from the critical point. The Reynolds number ranges for which cellular flows exist have been measured in the (Re_1, Re_2)-plane for both four-cell and five-cell flows. Moreover, the transition boundaries to the oscillatory flow states have been measured. All cellular flow states were found to exist in the neighbourhood of the diagonal $Re_1 = Re_2$.

Quantitative velocity and oscillation-amplitude profiles have been measured by LDV. These measurements confirm that the symmetries of the fully nonlinear cells for $Re_1 = Re_2$ are the same as those of the linear critical mode (Kuhlmann *et al.* 1997). Among these symmetries the point symmetry is preserved by the nonlinear oscillatory cells. Experimental imperfections (asymmetries) near the endwalls, however, led to a slightly disconnected bifurcation to cells for symmetrical driving ($Re_1 = Re_2$) in the present setup. The same imperfections are also responsible for small differences in the existence ranges of the steady Λ- and V-modes.

The steady elliptic instability in the two-sided lid-driven cavity is a result of the high strain in the basic (strongly merged) vortex flow (Kuhlmann *et al.* 1997). Considering a Rankine vortex in a multipolar strain field Eloy & Le Dizès (2001) have shown that this type of instability is a generic feature of strained vortices and the result of a triad resonance among Kelvin waves. Only little is known, however, about the secondary instabilities of steady three-dimensional strained vortices, i.e. the transition to time-dependence. Experiments by Eloy, Le Gal & Le Dizès (2000) have demonstrated that the stationary three-dimensional flow in an elliptically deformed rotating cylinder becomes unstable at higher Reynolds numbers to standing-wave oscillations. This is different from the earlier observations of Malkus (1989), but similar to the scenario in the present experiment. As was shown numerically by Mason & Kerswell (1999), the secondary instability of the steady and *weakly* nonlinear three-dimensional flow in elliptically deformed rotating cylinders can be caused by a time-dependent eigenmode of the basic elliptical flow. In the present experiments, however, the three-dimensional steady flow is *strongly* nonlinear and differs substantially from the basic two-dimensional flow when becoming time-dependent. This suggests that an explanation of the flow oscillations must be based on the full three-dimensional steady rather than on the unstable two-dimensional flow. It is an open question, moreover, if the transition to oscillations in the elliptical cylinder (Eloy *et al.* 2000) is of tricritical type, as in the cavity flow. For these reasons, full three-dimensional numerical simulations, including a detailed analysis of the spectral components of the oscillatory flow, would be beneficial to clarify the physical mechanism responsible for the transition to time-dependence.

This work has been supported by Deutsche Forschungsgemeinschaft under grant numbers Ku 896/5-1 and Ku 896/5-2. We gratefully acknowledge discussions with S. Albensoeder, who also provided figure 10(*b*), and we thank M. Murck for his assistance during the measurements.

REFERENCES

Aidun, C. K. & Triantafillopoulos, N. G. 1997 High-speed blade coating. In *Liquid Film Coating* (ed. S. F. Kistler & P. M. Schweizer), chap. 12d, p. 637. Chapman and Hall.

Aidun, C. K., Triantafillopoulos, N. G. & Benson, J. D. 1991 Global stability of a lid-driven cavity with throughflow: Flow visualization studies. *Phys. Fluids* A **3**, 2081–2091.

Albensoeder, S., Kuhlmann, H. C. & Rath, H. J. 2001*a* Multiplicity of steady two dimensional flows in two-sided lid-driven cavities. *Theor. Comput. Fluid Dyn.* **14**, 223–241.

Albensoeder, S., Kuhlmann, H. C. & Rath, H. J. 2001*b* Three-dimensional centrifugal-flow instabilities in the lid-driven cavity problem. *Phys. Fluids* **13**, 121–135.

Alleborn, N., Raszillier, H. & Durst, F. 1999 Lid-driven cavity with heat and mass transport. *Intl J. Heat Mass Transfer* **42**, 833–853.

Bayly, B. J. 1986 Three-dimensional instability of elliptical flow. *Phys. Rev. Lett.* **57**, 2160–2163.

Bayly, B. J., Orszag, S. A. & Herbert, T. 1988 Instability mechanisms in shear flow transition. *Annu. Rev. Fluid Mech.* **20**, 359–391.

Benjamin, A. S. & Denny, V. E. 1979 On the convergence of numerical solutions for 2-D flows in a cavity at large Re. *J. Comput. Phys.* **33**, 340–358.

Benson, J. D. & Aidun, C. K. 1992 Transition to unsteady nonperiodic state in a through-flow lid-driven cavity. *Phys. Fluids* A **4**, 2316–2319.

Bödewadt, U. T. 1940 Die Drehströmung über festem Grunde. *Z. Angew. Math. Mech.* **20**, 241–253.

Burggraf, O. R. 1966 Analytical and numerical studies of the structure of steady separated flows. *J. Fluid Mech.* **24**, 113–151.

Deville, M. Lê, T.-H. & Morchoisne, Y. 1992 *Numerical Simulation of 3-D Incompressible Unsteady Viscous Laminar Flows*. Notes on Numerical Fluid Mechanics, vol. 36. Braunschweig: Vieweg.

Ding, Y. & Kawahara, M. 1998 Linear stability of incompressible fluid flow in a cavity using finite element method. *Intl J. Numer. Meth. Fluids* **27**, 139–157.

Ding, Y. & Kawahara, M. 1999 Three-dimensional linear stability analysis of incompressible viscous flows using the finite element method. *Intl J. Numer. Meth. Fluids* **31**, 451–479.

Eloy, C. & Le Dizès, S. 2001 Stability of the Rankine vortex in a multipolar strain field. *Phys. Fluids* **13**, 660–676.

Eloy, C., Le Gal, P. & Le Dizès, S. 2000 Experimental study of the multiplolar vortex instability. *Phys. Rev. Lett.* **85**, 3400–3403.

Freitas, C. J., Street, R. L., Findikakis, A. N. & Koseff, J. R. 1985 Numerical simulation of three-dimensional flow in a cavity. *Intl J. Numer. Meth. Fluids* **5**, 561–575.

Herbert, T. 1988 Secondary instability of boundary layers. *Annu. Rev. Fluid Mech.* **20**, 487–526.

Koseff, J. R. & Street, R. L. 1984*a* The lid-driven cavity flow: A synthesis of qualitative and quantitative observations. *Trans. ASME: J. Fluids Engng* **106**, 390–398.

Koseff, J. R. & Street, R. L. 1984*b* On endwall effects in a lid-driven cavity flow. *Trans. ASME: J. Fluids Engng* **106**, 385–389.

Koseff, J. R. & Street, R. L. 1984*c* Visualization studies of a shear driven three-dimensional recirculating flow. *Trans. ASME: J. Fluids Engng* **106**, 21–29.

Koseff, J. R., Street, R. L., Gresho, P. M., Upson, C. D., Humphrey, J. A. C. & To, W.-M. 1983 A three-dimensional lid-driven cavity flow: Experiment and simulation. In *Proc. 3rd Intl Conf. on Numerical Methods in Laminar and Turbulent Flow* (ed. C. Taylor), pp. 564–581. Pimeridge Press.

Kuhlmann, H. C., Wanschura, M. & Rath, H. J. 1997 Flow in two-sided lid-driven cavities: Non-uniqueness, instabilities, and cellular structures. *J. Fluid Mech.* **336**, 267–299.

Kuhlmann, H. C., Wanschura, M. & Rath, H. J. 1998 Elliptic instability in two-sided lid-driven cavity flow. *Eur. J. Mech.* B/*Fluids* **17**, 561–569.

Lomb, N. R. 1976 Least-squares frequency analysis of unequally spaced data. *Astrophys. Space Sci.* **39**, 447–462.

MALKUS, W. V. R. 1989 An experimental study of global instabilities due to the tidal (elliptical) distortion of a rotating elastic cylinder. *Geophys. Astrophys. Fluid Dyn.* **48**, 123–134.

MASON, D. M. & KERSWELL, R. R. 1999 Nonlinear evolution of the elliptic innstability: an example of inertial wave breakdown. *J. Fluid Mech.* **396**, 73–108.

PAN, F. & ACRIVOS, A. 1967 Steady flows in rectangular cavities. *J. Fluid Mech.* **28**, 643–655.

PIERREHUMBERT, R. T. 1986 Universal short-wave instability of two-dimensional eddies in an inviscid fluid. *Phys. Rev. Lett.* **57**, 2157–2159.

PRASAD, A. K. & KOSEFF, J. R. 1989 Reynolds number and endwall effects on a lid-driven cavity flow. *Phys. Fluids* A **1**, 208–218.

PRESS, W. H., TEUKOLSKY, S. A., VETTERLING, W. T. & FLANNERY, B. P. 1992 *Numerical Receipes in C*. Cambridge University Press.

RAMANAN, N. & HOMSY, G. M. 1994 Linear stability of lid-driven cavity flow. *Phys. Fluids* **8**, 2690–2701.

RHEE, H. S., KOSEFF, J. R. & STREET, R. L. 1984 Flow visualization of recirculating flow by rheoscopic liquid and liquid crystal technique. *Exps. Fluids* **2**, 57–64.

SHANKAR, P. N. & DESHPANDE, M. D. 2000 Fluid mechanics in the driven cavity. *Annu. Rev. Fluid Mech.* **32**, 93–136.

STEFANOVIC, D. L. & STEFAN, H. G. 2000 Simulation of transient cavity flows driven by buoyancy and shear. *J. Hydraulic Res.* **38**, 181–195.

STEINBERG, V. & BRAND, H. R. 1984 Crossover from critical to tricritical behavior in a nonequilibrium system: The convective instability in a binary fluid mixture. *Phys. Rev.* A **30**, 3366–3368.

TRIANTAFILLOPOULOS, N. G. & AIDUN, C. K. 1990 Relationship between flow instability in short-dwell ponds and cross directional coat weight nonuniformities. *TAPPI J.* **73**, 127–136.

VISCHER, D. L. & HAGER, W. H. 1998 *Dam Hydraulics.* Wiley.

WULF, P., EGBERS, C. & RATH, H. J. 1999 Routes to chaos in wide-gap spherical couette flow. *Phys. Fluids* **11**, 1359–1372.